

A Refreshed Similarity-based Upsampler for Direct High-Ratio Feature Upsampling

Minghao Zhou, Hong Wang, Yefeng Zheng, *Fellow, IEEE*, and Deyu Meng, *Member, IEEE*

Abstract—Feature upsampling is a fundamental and indispensable ingredient of almost all current network structures for image segmentation tasks. Very recently, a popular similarity-based feature upsampling pipeline has been proposed, which utilizes a high-resolution (HR) feature as guidance to help upsample the low-resolution (LR) deep feature based on their local similarity. Albeit achieving promising performance, this pipeline has specific limitations in methodological designs: 1) HR query and LR key features are not well aligned in a controllable manner; 2) the similarity between query-key features is computed based on the fixed inner product form, lacking flexibility; 3) neighbor selection is coarsely operated on LR features, resulting in mosaic artifacts. These shortcomings make the existing methods along this pipeline primarily applicable to hierarchical network architectures with iterative features as guidance and they are not readily extended to a broader range of structures, especially for a direct high-ratio upsampling. Against these issues, we thoroughly refresh this pipeline and meticulously optimize every methodological design. Specifically, we firstly propose an explicitly controllable query-key feature alignment from both semantic-aware and detail-aware perspectives, and then construct a parameterized paired central difference convolution block for flexibly calculating the similarity between the well-aligned query-key features. Besides, we develop a fine-grained neighbor selection strategy on HR features, which is simple yet effective for alleviating mosaic artifacts. Based on these careful designs, we systematically construct a refreshed similarity-based feature upsampling framework named **ReSFU**. Comprehensive experiments substantiate that our proposed ReSFU is finely applicable to various types of architectures in a direct high-ratio upsampling manner, and consistently achieves satisfactory performance on different applications, including semantic segmentation, medical image segmentation, instance segmentation, and panoptic segmentation, showing superior generality and ease of deployment beyond the existing upsamplers. Codes are available at <https://github.com/zmhhmz/ReSFU>.

Index Terms—Feature upsampling, feature alignment, paired central difference convolution, high-ratio, semantic segmentation.

arXiv:2407.02283v1 [cs.CV] 2 Jul 2024

1 INTRODUCTION

As a fundamental ingredient in deep network architectures, feature upsampling aims to restore the spatial resolution of low-resolution (LR) features, which is widely used in image segmentation tasks, such as semantic segmentation [4], instance segmentation [5], and panoptic segmentation [6].

During the feature upsampling process, each high-resolution (HR) feature element is typically estimated by weighting its neighboring elements from the input LR feature. To generate the weights (also known as the upsampling kernels [2], [7]), in recent years, various upsampling research lines have been proposed. Specifically, bilinear and nearest-neighbor interpolation are the most widely-adopted feature upsampling methods, which are implemented based on hand-crafted weighting rules and often cause blurry effects. To enhance the flexibility of feature upsampling, some studies have developed different content-aware dynamic upsamplers [7]–[11]. For example, in [7], the authors devised a dynamic network to generate the upsampling kernel from LR features. Despite promising performance, they usually struggle to restore clear object boundaries due to the loss of fine-grained details in LR features.

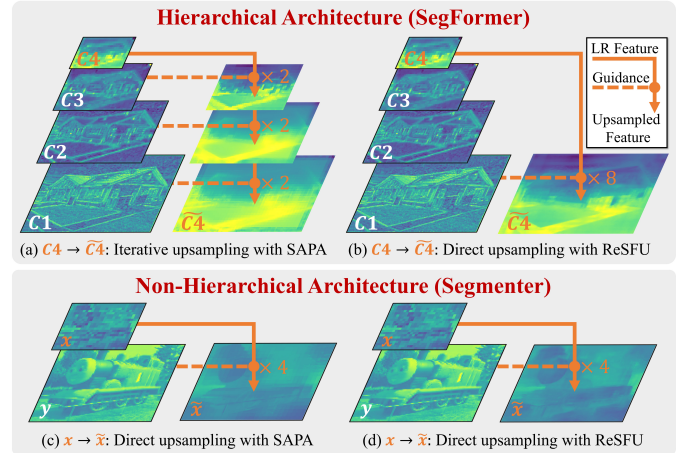


Figure 1: Upper: For the $\times 8$ upsampling from C_4 to \tilde{C}_4 in the hierarchical SegFormer [1], (a) SAPA [2] iteratively performs three $\times 2$ upsampling processes with intermediate features as guidance; (b) our ReSFU obtains clearer object boundaries in a direct $\times 8$ upsampling only with the guidance C_1 . Lower: For the $\times 4$ upsampling from x to \tilde{x} with the direct guidance of the shallow HR feature y in the non-hierarchical Segmenter [3], (c) SAPA suffers from mosaic artifacts, while (d) our ReSFU achieves better structural preservation. All the images are best viewed by zooming in on screen, especially to observe mosaic artifacts.

- Minghao Zhou and Deyu Meng are with School of Mathematics and Statistics and Ministry of Education Key Lab of Intelligent Networks and Network Security, Xi'an Jiaotong University, Xi'an 710049, China. Work was done when Minghao Zhou interned in Tencent YouTu Lab. (E-mail: woshizhouminghao@stu.xjtu.edu.cn, dymeng@mail.xjtu.edu.cn)
- Hong Wang and Yefeng Zheng are with Tencent YouTu Lab, Shenzhen, China. (E-mail: {hazelhwang, yefengzheng}@tencent.com)

Against this issue, a novel similarity-based feature upsampling pipeline SAPA [2] has been proposed, which utilizes an HR feature y as the guidance to help accomplish

the upsampling process from the LR feature \mathbf{x} to the HR one $\tilde{\mathbf{x}}$. Taking the representative base version of SAPA as an example, the HR feature element $\tilde{\mathbf{x}}_i$ at pixel i is estimated as (see Sec. 3 for more details):

$$\tilde{\mathbf{x}}_i = \underbrace{\text{Softmax}(\mathbf{q}_i \mathbf{k}_{\mathcal{N}(i)}^T)}_{\text{upsampling kernel}} \mathbf{x}_{\mathcal{N}(i)}, \quad (1)$$

where the HR query \mathbf{q} and the LR key \mathbf{k} are linear projections of \mathbf{y} and \mathbf{x} , respectively; $\mathcal{N}(i)$ is the neighborhood of i ; the upsampling kernel is computed on the inner produced-based similarity between the query-key pair. We can easily see that the entire upsampling framework along the similarity-based pipeline is closely related to the design of three main components: ❶ the acquisition of query-key features; ❷ the similarity calculation manner between the query-key pair; ❸ the neighbor selection $\mathcal{N}(i)$.

Albeit obtaining impressive success, we carefully delve into this pipeline and find that each of the aforementioned components in SAPA still suffers from unresolved issues. Specifically, ❶ considering that the HR guidance feature \mathbf{y} is usually shallower than the LR deep feature \mathbf{x} , only with the content-agnostic linear projection operation, the generated \mathbf{q} and \mathbf{k} are generally not well semantically aligned in a controllable manner. This would adversely interfere with the subsequent similarity calculation; ❷ The inner product-based similarity calculation manner in Eq. (1) lacks enough flexibility and often results in blurry effects in the upsampled features (see $\tilde{C}4$ in Fig. 1 (a)); ❸ From Eq. (1), the neighbor selection $\mathcal{N}(i)$ is coarsely executed on LR features \mathbf{k} and \mathbf{x} , which would incur mosaic artifacts, especially in a direct high-ratio upsampling (see $\tilde{\mathbf{x}}$ in Fig. 1 (c)).

These three methodological design limitations weaken the potential application of SAPA, making it usually only applicable to iterative $\times 2$ upsampling structures with hierarchical guidances but less suitable for direct high-ratio upsampling without iterative features as guidance. For instance, for the hierarchical architecture SegFormer [1] with four levels of features as shown in Fig. 1 (a), to accomplish the $\times 8$ upsampling from $C4$ to $\tilde{C}4$, SAPA, as well as other existing feature upsampling methods [7], [12], [13], performs three consecutive $\times 2$ upsampling processes with $C3$, $C2$, and $C1$ as guidance features, respectively. Such an iterative pattern definitely leads to the laborious deployment of more upsampling modules. Besides, for the non-hierarchical structures, such as Segmenter [3] in Fig. 1 (c), the deep LR feature \mathbf{x} requires a direct $\times 4$ upsampling under the guidance of a shallow HR feature \mathbf{y} . Without iterative guidance features, the upsampled feature $\tilde{\mathbf{x}}$ exhibits adverse visual artifacts. These issues generally exist in most of the current feature upsampling methods (see Sec. 5.2). Faced with this tricky scenario, is it possible to build an *architecture-agnostic* feature upsampling framework that is applicable to different types of network architectures and can always achieve satisfactory effects in *direct high-ratio upsampling* without complicated iterative processes?

To answer this question, in this paper, we meticulously refresh the pipeline in Eq. (1) and carefully optimize the involved three main components one by one. Then we propose a Refreshed Similarity-based Feature Upsampling framework, called ReSFU, with higher flexibility and better

universality, which can be easily embedded in a direct high-ratio upsampling manner for different architectures as shown in Figs. 1 (b) and (d). Specifically, our contributions are mainly four-fold:

1) Firstly, we propose an explicitly controllable algorithm to finely align query-key features from both semantic-aware and detail-aware perspectives. Concretely, we utilize guided filter (GF) [14] to explicitly optimize the original linearly-projected HR query \mathbf{q} and execute a controllable transformation on it to promote semantic alignment with the key. Meanwhile, we further investigate the HR query \mathbf{q} itself and adopt an explicit Gaussian smoothing to help accomplish the HR feature self-alignment for better detail preservation. Such careful query-key alignment designs facilitate more accurate similarity computation and make it possible to flexibly select the guidance features, such as the cross-level guided high-ratio upsampling from $C4$ to $\tilde{C}4$ in Fig. 1 (b) without complicated iterative procedures as in SAPA.

2) Secondly, for the well-aligned pairs, we propose a paired central difference convolution (PCDC) to inherently capture the local relevance between the query-key features, and then correspondingly construct a parameterized PCDC-Block to flexibly calculate the similarity between every pair. Compared with the non-parametric inner product in Eq. (1), the proposed PCDC-Block can help better ameliorate blurry artifacts, as experimentally validated by comparing $\tilde{C}4$ in Figs. 1 (a) and (b).

3) Thirdly, we propose a fine-grained neighbor selection strategy by selecting the neighbors $\mathcal{N}(i)$ of every HR pixel i based on the bilinearly-upsampled HR version of the LR features \mathbf{k} and \mathbf{x} . Such a simple yet effective design introduces no extra parameters and can be seamlessly incorporated into our ReSFU framework with ease, which evidently reduces mosaic artifacts even in case of the direct high-ratio upsampling, as presented in Fig. 1 (d).

4) Finally, by correspondingly replacing the three main components in Eq. (1) with our proposed aforementioned three designs, we systematically build ReSFU. Extensive experiments comprehensively demonstrate that compared to baselines, the proposed ReSFU consistently (i) achieves better results in direct high-ratio upsampling on various types of architectures, and (ii) shows superior generality across different segmentation tasks, such as, semantic/instance/panoptic segmentation, and across various types of datasets, including natural and medical images. Moreover, we provide detailed model visualizations and ablation studies to verify the working mechanism underlying ReSFU.

The rest of the paper is organized as follows: Sec. 2 introduces the related work. Sec. 3 reformulates and analyzes the current similarity-based feature upsampling framework based on experimental visualization. Sec. 4 presents the specific designs of our proposed ReSFU. Sec. 5 substantiates the effectiveness of our method through comprehensive experiments. Finally, Sec. 6 concludes the paper.

2 RELATED WORK

2.1 Feature Upsampling

Guidance-Free Upsampling Methods. Nearest neighbor and bilinear interpolation are two widely adopted feature

upsampling methods that are implemented based on pre-defined distance-aware rules. For higher flexibility, several techniques have been proposed to learn the upsampling kernels in an end-to-end manner, such as Deconvolution [15]. PixelShuffle [8] is also commonly adopted to perform efficient sub-pixel convolution for upsampling, which rearranges the elements within the channel dimension to increase the spatial resolution. Although these approaches and their subsequent improvements [9]–[11] achieve certain performance gains, they cannot dynamically adjust the upsampling kernels based on feature contents.

Recently, CARAFE [7], [16] firstly proposed to dynamically learn the upsampling kernels from the to-be-upsampled LR features. Alternatively, DySample [13] generated the point sampling offsets of the upsampled pixels from the deep LR features. In these methods, the upsampling procedure can be dynamically adjusted based on deep LR features, further improving the upsampling flexibility. However, due to the loss of fine-grained details in deep LR features and the lack of HR guidance features, the upsampled features achieved by these guidance-free methods usually have blurry effects.

Guidance-based Upsampling Methods. To enhance the detail recovery in upsampled features, a research line has been proposed to utilize the information from shallow HR features to guide the upsampling process [17], [18]. For example, IndexNet [19], A2U [20], and FADE [12] were developed in succession to generate the dynamic upsampling kernels from both the HR guidance and LR deep features. Along this line, SAPA [2], [21] proposed to generate the upsampling kernels by modelling the local similarity between HR guidance and LR deep features. FeatUp [22] introduced a multi-view consistency learning framework based on the stacked parameterized joint bilateral upsampler (JBU) [23] and an implicit multilayer perceptron (MLP) upsampler, respectively. The implicit version requires inference-time training, which is extremely time-consuming. In this paper, driven by the competitive performance of the latest representative SAPA, we follow its similarity-based feature upsampling framework, thoroughly analyze the inherent characteristics, and then specifically propose optimization designs for better upsampling effects.

2.2 Convolution Operators

To adapt to different application needs, many convolution operators have emerged as replacements for standard convolution in recent years [24]. For instance, based on local binary pattern [25], LBC [26], [27] proposed a set of fixed sparse pre-defined binary convolutional filters, which can significantly save the computational overhead while approximating the capability of traditional convolutional layers. CDC [28]–[31] constructed a specific convolution based on central difference maps to capture boundary information. Along this line, PDC [32], [33] further considered the difference between different pixel pairs and SDC [34] introduced both central difference and similarity into the convolution design. They have been effectively applied to vision tasks, such as face anti-spoofing, edge detection, and semantic segmentation. These convolution operators are usually executed on a *single* input feature. However, in this

paper, we aim to novelly design a convolution operation for flexible similarity computation between a *pair* of content-aligned input features.

2.3 Image Segmentation

In this field of computer vision, image segmentation is a fundamental task in widespread applications, such as medical imaging [35] and autonomous driving [36], which includes semantic segmentation [4], instance segmentation [5], and panoptic segmentation [6]. The goal is to predict semantic labels or delineate individual instances of objects in images, helping provide essential scene understanding.

Against these tasks, various network architectures have been constructed in the past few years. For example, for scene parsing and semantic segmentation of natural images, CNN-based PSPNet [37] and DeepLab-V3+ [38] achieved prominent outcomes by utilizing atrous convolutions and spatial pyramid pooling to effectively capture multi-scale information. Inspired by the successful application of Transformer in computer vision [39], [40], various Transformer-based network architectures have been proposed for semantic segmentation, such as Segmenter [3], SegFormer [1], and SegNeXt [41], which demonstrated impressive performance by leveraging the power of long-range dependencies. For instance segmentation, Mask R-CNN [42] and its variants [43]–[45] have been widely used due to the robust performance. For panoptic segmentation, the representative Panoptic FPN [6], UPSNet [46], and EfficientPS [47] sequentially consist of two procedures, *i.e.*, semantic segmentation and instance segmentation. Besides, the U-shape network architectures [35], [48]–[50] have been broadly utilized for medical image segmentation. Recently, researchers [51]–[53] explored an alternative approach to the traditional pixel-wise classification and proposed to adopt a Transformer-based decoder for mask classification, which shows remarkable performance in different image segmentation tasks.

For these network architectures, the spatial size of intermediate features usually gradually reduces to efficiently encode high-level semantic information, and thus feature upsampling is an indispensable module for the final prediction. In this paper, we aim to design a general feature upsampling framework, which can be easily encapsulated into various structures for more accurate segmentation.

3 REVISITING SIMILARITY-BASED FEATURE UPSAMPLING PIPELINE

In this section, we carefully reformulate and delve into the current similarity-based feature upsampling pipeline.

Given an LR deep feature $\mathbf{x} \in \mathbb{R}^{hw \times C}$ and an HR guidance feature $\mathbf{y} \in \mathbb{R}^{HW \times c}$,¹ the existing similarity-based feature upsampling framework SAPA [2], [21] aims to upsample \mathbf{x} to an HR deep feature $\tilde{\mathbf{x}} \in \mathbb{R}^{HW \times C}$ under the guidance of \mathbf{y} . Specifically, for each HR pixel $i \in \{1, \dots, HW\}$, the HR deep feature element $\tilde{x}_i \in \mathbb{R}^C$ is generally estimated by weighting its neighboring LR deep feature elements based on an upsampling kernel $\text{Softmax}(\mathbf{s}_i)$ as:

$$\tilde{\mathbf{x}}_i = \text{Softmax}(\mathbf{s}_i) \mathbf{x}_{\mathcal{N}(i)}, \quad (2)$$

¹For simplicity, we aggregate the spatial dimensions $H \times W$ as HW .

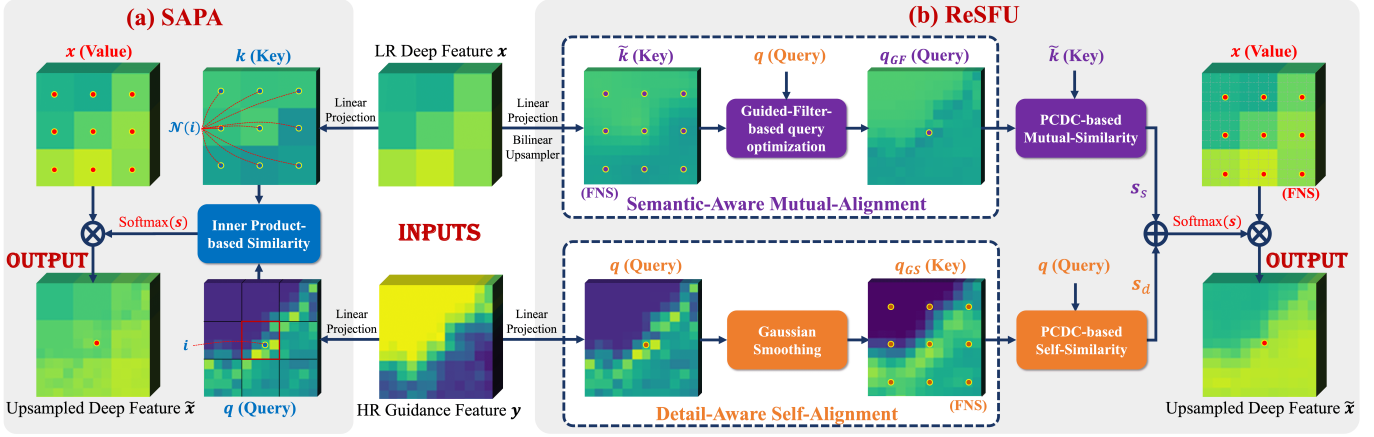


Figure 2: Targeting every part in (a) SAPA, (b) our ReSFU proposes specific optimization designs, *i.e.*, controllable query-key feature alignment from both semantic-aware and detail-aware perspectives, paired central difference convolution (PCDC)-based flexible similarity calculation between aligned query-key pairs, and fine-grained neighbor selection (FNS). Here the visualization is experimentally based on Segformer-S for a $\times 4$ feature upsampling from x to \tilde{x} . *Best viewed with zoom-in.*

where $x_{\mathcal{N}(i)} \in \mathbb{R}^{K^2 \times C}$ denotes the neighboring LR feature elements of pixel i ; $|\mathcal{N}(i)| = K^2$ is the number of neighboring LR pixels with a pre-defined kernel size K ; $s_i \in \mathbb{R}^{K^2}$ is the similarity scores assigned to the K^2 neighbors of pixel i . In the representative base version of SAPA [2], s_i is computed as:

$$s_i \triangleq \text{sim}(q_i, k_{\mathcal{N}(i)}) \triangleq q_i k_{\mathcal{N}(i)}^T, \quad (3)$$

where q and k are linear projections of y and x , respectively, with D channels; $q_i \in \mathbb{R}^D$ is the i -th feature element of $q \in \mathbb{R}^{HW \times D}$; $k_{\mathcal{N}(i)} \in \mathbb{R}^{K^2 \times D}$ represents the K^2 neighboring feature elements of pixel i in $k \in \mathbb{R}^{hw \times D}$; $\text{sim}(\cdot, \cdot)$ is a general similarity function, designed as the inner product between q_i and $k_{\mathcal{N}(i)}$ in SAPA. We regard q , k , and x as the HR query, LR key, and LR value features, respectively.

As seen, the entire similarity-based feature upsampling pipeline is strongly associated with the design of three main parts: ❶ query-key feature acquisition for facilitating the computation of similarity s_i ; ❷ the similarity function $\text{sim}(\cdot, \cdot)$; ❸ neighbor selection $\mathcal{N}(i)$. For better understanding, based on the backbone Segformer-S with a direct $\times 4$ upsampling for the last-layer feature under the guidance of a shallow feature (see Fig. 10), we experimentally visualize SAPA in Fig. 2 (a) and identify the following issues:

1) **Uncontrollable Query-Key Alignment.** In such a direct high-ratio upsampling case, the HR guidance feature y is relatively shallow and it generally contains low-level information, such as texture patterns, while the LR deep feature x usually contains high-level semantics [40], [54]. Since the linear projection operation with fixed weights is not sensitive to the content of either y or x , the linearly-projected query and key cannot be well-aligned in the feature space without extra control, which would seriously mislead the subsequent similarity computation.

2) **Inflexible Similarity Computation.** The conventional inner product operation in Eq. (3) is non-parametric and lacks flexibility in capturing the relations between the query and key. Directly adopting this inner product form would cause that within a small local region $\mathcal{N}(i)$, the computed K^2 scores $q_i k_{\mathcal{N}(i)}^T$ are close to each other (see Fig. 6 (a)). This would consequently generate an overly smooth upsampling

kernel, leading to blurry artifacts in the upsampled \tilde{x} .

3) **Coarse Neighbor Selection.** From Eqs. (2) and (3), the neighbors $\mathcal{N}(i)$ of pixel i are correspondingly selected on the LR key k and the LR value x , respectively. This manner is coarse. Specifically, taking the neighbor selection on k as an example, as shown in Fig. 2 (a), for the $\times 4$ upsampling, all the sixteen pixels in the 4×4 red box marked in q share identical neighbors, *i.e.*, the nine pixels marked in k . On the other hand, for two adjacent pixels i and j in q from two different 4×4 boxes, the selected neighbors $\mathcal{N}(i)$ and $\mathcal{N}(j)$ in k would differ abruptly. Such a grid-wise neighbor selection strategy on LR features often results in mosaic artifacts in \tilde{x} , especially for a direct high-ratio upsampling.

These limitations in methodological designs constrain that most of the existing feature upsampling methods along this similarity-based pipeline are always injected into network backbones in a step-by-step $\times 2$ upsampling manner. They are generally suitable for hierarchical architectures with the iterative upsampling process, like SegFormer in Fig. 1 (a), and are difficult to be extended to more types of backbones, such as non-hierarchical architectures with a direct high-ratio upsampling, like Segformer in Fig. 1 (c).

4 METHOD

Motivated by the analysis in Sec. 3, in this section, we aim to refresh the current similarity-based feature upsampling framework by carefully optimizing every involved component in Eqs. (2) and (3), including query-key alignment, similarity computation, and neighbor selection. Then we correspondingly construct a more flexible and universal upsampling framework, called ReSFU, which has the potential to adapt to various network structures.

Specifically, as shown in Fig. 2 (b), we first propose a controllable query-key feature alignment method from both semantic-aware and detail-aware perspectives. Then, we design a specific paired central difference convolution (PCDC) block for flexibly calculating the similarity between the aligned query-key pairs. Finally, we devise a fine-grained neighbor selection (FNS) strategy to alleviate mosaic artifacts. For each part, the detailed designs are given below.

4.1 Explicitly Controllable Query-Key Alignment

From [40], [54], an HR guidance feature \mathbf{y} from a shallow layer usually captures more detail-related information while the LR deep feature \mathbf{x} encodes more semantic-related information. Thus, we informally refer to \mathbf{y} (and its linear projection, the query feature \mathbf{q}) and \mathbf{x} (and its linear projection, the key feature \mathbf{k}) as residing in the *detail space* and the *semantic space*, respectively, as presented in Fig. 3.

Confronted with the representational discrepancy between the detail and semantic spaces, it is inaccurate to directly calculate the similarity score between the original query-key feature pair, *i.e.*, \mathbf{q} and \mathbf{k} , across different spaces. To fully capture and exploit the relations among different neighboring pixels that share similar information both at the detail and semantic levels for guiding the upsampling process, we propose a two-pronged approach to explicitly transform the original features and generate two query-key pairs aligned in detail space and semantic space, respectively, to facilitate accurate similarity computation. Please refer to the lower row of Fig. 3 for the overall design.

4.1.1 Semantic-Aware Mutual-Alignment

Firstly, our goal is to project the original query \mathbf{q} into the semantic space so that it can better align with the key feature \mathbf{k} in the semantic space, while also preserving the structural details in the detail space. To this end, inspired by the guided filter (GF) [14], [55], we propose to linearly transform \mathbf{q} in every local window for detail preservation while minimizing the distance between the transformed query and the key \mathbf{k} for the mutual-alignment in the semantic space. In this manner, the structural information of \mathbf{q} can be efficiently integrated with the semantic information of \mathbf{k} into the transformed query [14].

Mathematically, let $\mathbf{q}_{GF} \in \mathbb{R}^{HW \times D}$ be the transformed query and each of its element $(\mathbf{q}_{GF})_{id}$ can be estimated via solving the following optimization problem [14]:

$$\begin{aligned} \min_{\mathbf{m}_{jd}, \mathbf{n}_{jd}} \sum_{i \in I_j} \left(\left((\mathbf{q}_{GF})_{id} - \tilde{\mathbf{k}}_{id} \right)^2 + \epsilon \mathbf{m}_{jd}^2 \right), \\ \text{s.t. } (\mathbf{q}_{GF})_{id} = \mathbf{m}_{jd} \mathbf{q}_{id} + \mathbf{n}_{jd}, \forall i \in I_j, \end{aligned} \quad (4)$$

where $(\mathbf{q}_{GF})_{id}$, \mathbf{q}_{id} , and $\tilde{\mathbf{k}}_{id}$ are the feature elements of \mathbf{q}_{GF} , \mathbf{q} , and $\tilde{\mathbf{k}}$ at pixel i and channel d , respectively; $\tilde{\mathbf{k}} \in \mathbb{R}^{HW \times D}$ is the bilinearly upsampled HR result of the original LR key \mathbf{k} ; $d \in \{1, \dots, D\}$; \mathbf{m}_{jd} and \mathbf{n}_{jd} are linear coefficients for pixel j at channel d ; I_j is a square window with radius r centered at pixel $j \in \{1, \dots, HW\}$; and ϵ is a small regularization weight. In experiments, the radius r is experimentally set to 8 and ϵ is set to 0.001. Please note that for element-wise minimization computation in Eq. (4), we adopt the upsampled key feature $\tilde{\mathbf{k}}$ for keeping the same size with \mathbf{q}_{GF} , which also belongs to the semantic space.

From [56], the explicit solution of Eq. (4) can be easily derived as:

$$\begin{aligned} \mathbf{m}_{jd} &= \frac{\frac{1}{|I_j|} \sum_{i \in I_j} \mathbf{q}_{id} \tilde{\mathbf{k}}_{id} - \mu_{jd}^q \mu_{jd}^k}{\sigma_{jd}^2 + \epsilon}, \\ \mathbf{n}_{jd} &= \mu_{jd}^k - \mathbf{m}_{jd} \mu_{jd}^q, \end{aligned} \quad (5)$$

where μ_{jd}^q and σ_{jd}^2 are the mean and variance of \mathbf{q}_{id} in the local window I_j ; μ_{jd}^k is the mean of $\tilde{\mathbf{k}}_{id}$ in I_j , expressed

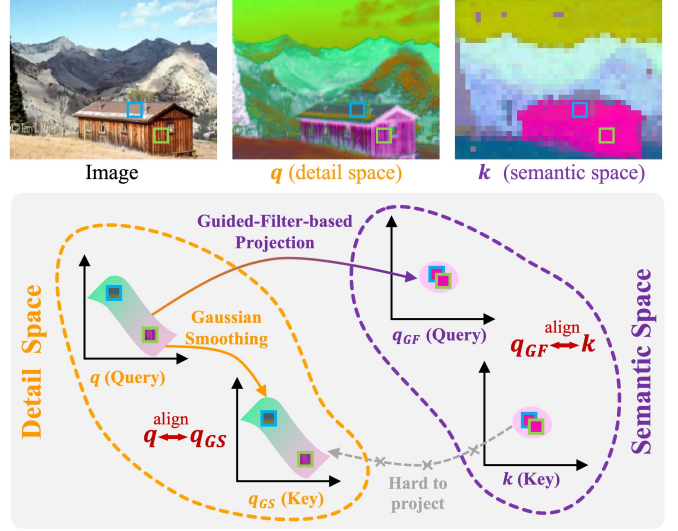


Figure 3: Upper: For the two regions marked by blue and green boxes, *i.e.*, the roof and the wall of the house, they have similar features in the semantic space but significantly differ in the detail space. Lower: The overall concept of our two-pronged approach to construct the aligned query-key pair in the semantic space and detail space, respectively.

as $\mu_{jd}^k = \frac{1}{|I_j|} \sum_{i \in I_j} \tilde{\mathbf{k}}_{id}$; and $|I_j|$ is the number of pixels contained in the local window I_j , which is r^2 .

Since a pixel i is involved in different overlapping window I_j that covers the pixel i , $(\mathbf{q}_{GF})_{id}$ would change with these local windows. Following [14], by averaging all these overlapping local windows I_j , we can get the final transformed query as:

$$(\mathbf{q}_{GF})_{id} = \bar{\mathbf{m}}_{id} \mathbf{q}_{id} + \bar{\mathbf{n}}_{id}, \quad (6)$$

where $\bar{\mathbf{m}}_{id} = \frac{1}{|I_i|} \sum_{j \in I_i} \mathbf{m}_{jd}$ and $\bar{\mathbf{n}}_{id} = \frac{1}{|I_i|} \sum_{j \in I_i} \mathbf{n}_{jd}$.

As seen, the optimized query \mathbf{q}_{GF} is explicitly derived on the basis of the original query \mathbf{q} and key \mathbf{k} , achieving the controllable alignment with key in the semantic space. From Eq. (3), for the explicitly optimized query-key pair \mathbf{q}_{GF} and $\tilde{\mathbf{k}}$, the similarity $(s_s)_i$ for pixel i is calculated as:

$$(s_s)_i \triangleq \text{sim}((\mathbf{q}_{GF})_i, \tilde{\mathbf{k}}_{N(i)}). \quad (7)$$

We call $s_s \in \mathbb{R}^{HW \times K^2}$ as semantic-aware mutual similarity.

Remark 1: From the visualization in Fig. 2 (b), we can clearly observe that: 1) compared to the original linearly-projected query \mathbf{q} , the explicitly optimized query \mathbf{q}_{GF} exhibits a stronger semantic resemblance to the key $\tilde{\mathbf{k}}$. This can promote more accurate semantic-aware similarity computation of s_s for better performance (see Sec. 5.3.2); 2) \mathbf{q}_{GF} effectively preserves the original intricate structures in \mathbf{q} , which would guide the upsampling to achieve a higher structural fidelity in the upsampled feature $\tilde{\mathbf{x}}$ (also see Fig. 16). All these advantages finely comply with our design motivation for Eq. (4) and substantiate its rationality.

4.1.2 Detail-Aware Self-Alignment

In addition to the semantic space, we also seek to fully exploit the structural information in the detail space and generate the aligned query-key pair in this space for better guiding the upsampling process. Unfortunately, unlike the

semantic space, it is hard to project the key feature into the detail space to achieve the query-key mutual-alignment. This is because that deep semantic information is more abstract and the features in the detail space generally reside in a higher-dimensional manifold than that in the semantic space. For example, in Fig. 3, the blue and green boxes highlight areas belong to the same semantic category, *i.e.*, house, with closer distance in the semantic space. However, they possess highly diverse detail information, *i.e.*, roof and wall, with farther distance in the detail space. In this case, it is hardly feasible to find a proper projection to finely transform the original key \mathbf{k} to the detail space, which can reproduce the level of detail variations in the query feature.

Confronted with the above issue, we propose a detail-aware self-alignment approach that exploits the query in the detail space to generate the aligned key feature for the space. One intuitive way is to directly regard \mathbf{q} as both the query and key features in the detail space. However, we further analyze that to avoid significant fluctuations in local similarity scores, the real key feature is generally expected to have the property of smoothness [39], [57], like the original key \mathbf{k} in the semantic space containing minimal semantically irrelevant noises. Motivated by this analysis, we propose to execute a simple Gaussian smoothing operator on \mathbf{q} to suppress high-frequency noisy details to obtain a smoothed key feature $\mathbf{q}_{GS} \in \mathbb{R}^{HW \times D}$ in the detail space.

Then, for pixel i , the self-similarity $(s_d)_i$ for the aligned pair \mathbf{q} and \mathbf{q}_{GS} in the detail space is computed as:

$$(s_d)_i \triangleq \text{sim}(\mathbf{q}_i, (\mathbf{q}_{GS})_{\mathcal{N}(i)}), \quad (8)$$

where $\mathbf{q}_{GS} = \mathbf{f} \otimes \mathbf{q}$ and $\mathbf{f} \in \mathbb{R}^{3 \times 3}$ represents the Gaussian filter with the unit standard deviation. Here $s_d \in \mathbb{R}^{HW \times K^2}$ is the detail-aware self-similarity.

As seen, on the basis of the original linearly-projected query \mathbf{q} and \mathbf{k} , we introduce explicit optimization controls to further make them better aligned from both semantic-aware and detail-aware perspectives. Correspondingly, for our method, the similarity score s_i in Eq. (2) is designed as:

$$s_i = (s_s)_i + (s_d)_i. \quad (9)$$

Please note that the similarity function $\text{sim}(\cdot, \cdot)$ for computing s_s and s_d is implemented based on learnable parameterized form as formulated in Sec. 4.2 below. Hence, it is unnecessary to assign extra weighting coefficients on these two terms s_s and s_d in Eq. (9).

Remark 2: 1) The rationality of the detail-aware self-alignment can be explained from another perspective. Specifically, it is well-acknowledged that within a small local region of a relatively shallow feature, if two pixels exhibit similarity in detail structures, there is a high likelihood that they should possess similar semantics in the upsampled feature $\tilde{\mathbf{x}}$ [58]. Thus, it is reasonable to exploit the self-similarity on query \mathbf{q} itself for guiding the upsampling process; 2) The incorporation of the detail-aware similarity favorably encourages fine-grained detail preservation and the smoothed key generation design would indeed bring some performance improvement as validated in Sec. 5.3.2.

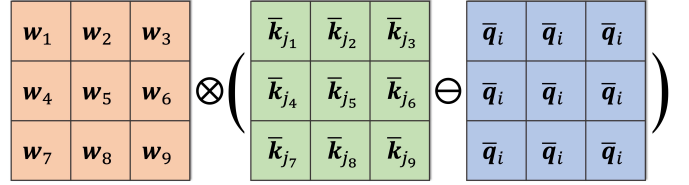


Figure 4: Illustration of the PCDC operation in Eq. (11) for any input channel d and any output channel l where the bias term \mathbf{b}_l is omitted for brevity. Here \otimes is the convolution operation and \ominus is the element-wise subtraction operation.

4.2 PCDC for Flexible Similarity Calculation

To compute s_s and s_d in Eq. (9), instead of adopting the fixed inner product-based manner for $\text{sim}(\cdot, \cdot)$ in [2], [21], here we aim to specifically design a parameterized convolution operation to flexibly model the inherent relevance between every query-key pair, *i.e.*, \mathbf{q}_{GF} and $\bar{\mathbf{k}}$, \mathbf{q} and \mathbf{q}_{GS} , for more accurate similarity calculation.

4.2.1 Paired Central Difference Convolution

For a vanilla convolution layer with G groups, given an arbitrary input $\tilde{\mathbf{x}} \in \mathbb{R}^{HW \times D}$ with D input channels, each element v_{il} in the convolution result $\mathbf{v} \in \mathbb{R}^{HW \times L}$ with L output channels is calculated by:

$$v_{il} = \sum_{d=gD/G}^{(g+1)D/G-1} \sum_{n=1}^{K^2} \mathbf{w}_{n\bar{d}l} \tilde{\mathbf{x}}_{j_n d} + \mathbf{b}_l, \quad j_n \in \mathcal{N}(i), \quad (10)$$

where i is the pixel index; the output channel index $l \in \{0, \dots, L-1\}$; $g = \lfloor \frac{i}{L} \rfloor$ is the group index ranging from 0 to $G-1$; d is the input channel index; $j_n \in \mathcal{N}(i)$ indexes a neighbor of the pixel i , with $n = 1, \dots, K^2$; $\mathbf{w}_{n\bar{d}l}$ is an element of $\mathbf{w} \in \mathbb{R}^{K^2 \times D/G \times L}$ representing the grouped convolution weights; the index $\bar{d} = d \% (\frac{D}{G})$, where $\%$ is the modulo operation; $\mathbf{b} \in \mathbb{R}^L$ is the bias.

Inspired by the ability of central difference convolution [28] in combining the flexibility of learnable convolution and the awareness of local gradient information, here we propose a paired central difference convolution (PCDC) to capture the relations between the query and key features. Specifically, following the framework of the vanilla grouped convolution in Eq. (10), we replace its input $\tilde{\mathbf{x}}$ with the ‘‘paired central difference’’ between any aligned query-key pair, $\bar{\mathbf{q}}$ and $\bar{\mathbf{k}}$, and then obtain the PCDC output \mathbf{v} as:

$$v_{il} = \sum_{d=gD/G}^{(g+1)D/G-1} \sum_{n=1}^{K^2} \mathbf{w}_{n\bar{d}l} (\bar{k}_{j_n d} - \bar{q}_{id}) + \mathbf{b}_l, \quad j_n \in \mathcal{N}(i). \quad (11)$$

For a better understanding of the working mechanism of the proposed PCDC, we provide a visual illustration of Eq. (11) with the kernel size K as 3. As observed from Fig. 4, through the learnable convolution weights, the differences between the central query element \bar{q}_i and its neighboring key elements \bar{k}_{j_n} can be well captured and flexibly processed. Naturally, the PCDC output \mathbf{v} has the capability to encode the local similarity information between $\bar{\mathbf{q}}$ and $\bar{\mathbf{k}}$.

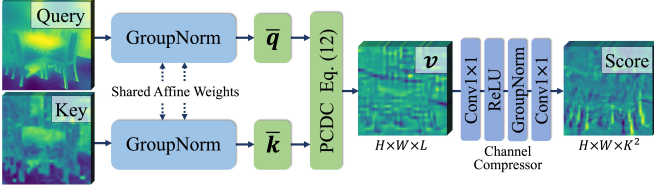


Figure 5: Illustration of PCDC-Block for similarity calculation between the aligned query-key pair.

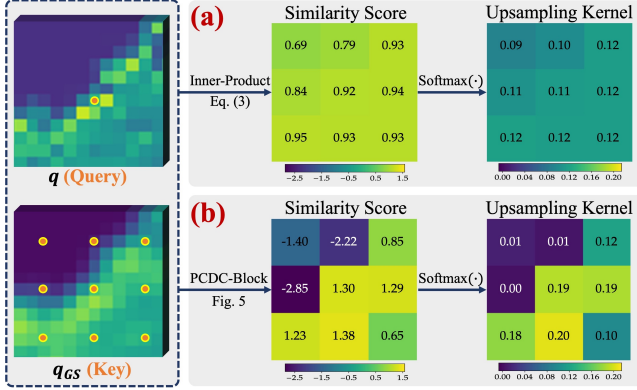


Figure 6: Visualization of similarity scores and softmax values (*i.e.*, upsampling kernels) computed through (a) inner product in Eq. (3) and (b) PCDC-Block illustrated in Fig. 5.

Equivalently, Eq. (11) can be decomposed as:

$$\begin{aligned}
 v_{il} = & \sum_{d=gD/G}^{(g+1)D/G-1} \sum_{n=1}^{K^2} w_{nd\bar{l}} \bar{k}_{j_n d} \\
 & - \sum_{d=gD/G}^{(g+1)D/G-1} \bar{q}_{id} \left(\sum_{n=1}^{K^2} w_{nd\bar{l}} \right) + b_l, \quad j_n \in \mathcal{N}(i).
 \end{aligned} \quad (12)$$

We can find that the proposed PCDC inherently consists of a vanilla grouped convolution on \bar{k} with weight w (the first term in Eq. (12)), and a 1×1 convolution on \bar{q} with the weight as the aggregation of w in the spatial dimension (the second term in Eq. (12)). These operations can be easily and efficiently implemented based on PyTorch [59] (see the pseudocode in the supplementary material).

4.2.2 PCDC-Block for Similarity Calculation

Based on the capability of the proposed PCDC in capturing the local similarity between the query-key pair, here we construct a PCDC-Block to finally implement the function $\text{sim}(\cdot, \cdot)$ for similarity computation as given in Fig. 5.

Concretely, for each aligned query-key pair, *i.e.*, q_{GF} and \bar{k} , q and q_{GS} , they are first separately input to a group normalization layer with shared affine parameters to get the normalized query-key pair \bar{q} and \bar{k} . Then the normalized pair is passed through a PCDC computation layer, *i.e.*, Eq. (12), to obtain the intermediate result v . Then by feeding v to a channel compressor to transform the channel number from L to K^2 , we can get the corresponding similarity scores for every query-key pair, *i.e.*, s_s and s_d . Here the channel compressor is sequentially composed of a 1×1 convolution layer, a ReLU layer, a group normalization layer, and a 1×1 convolution layer, where these two convolution layers are both with 4 groups and the intermediate channel size is 128.

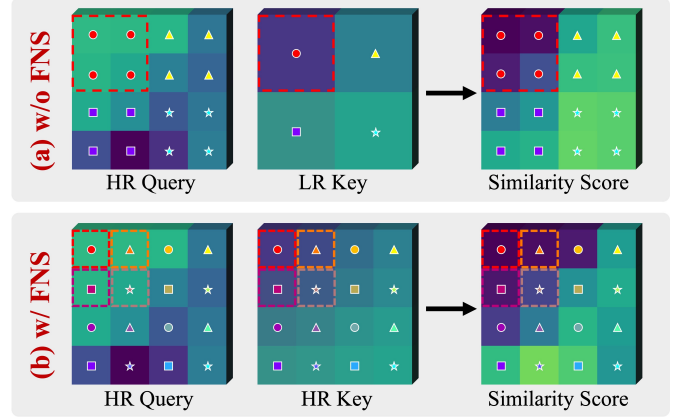


Figure 7: Illustration of the query-key similarity calculation process under different neighborhood selection strategies for $\mathcal{N}(i)$: (a) without FNS and (b) with FNS. Here the kernel size $K = 1$ and the upsampling ratio is 2. Pixels with the same color and shape in the query and key are paired for computing the similarity scores.

To better understand the inherent advantages of our proposed PCDC-Block over the traditional inner product-based form in Eq. (3) for similarity computation, here we provide an intuitive experimental display with the kernel size K as 3. Fig. 6 compares the similarity scores computed by these two methods for an image patch at pixels indicated by the orange circles in q and q_{GS} . As seen, even along clear object boundaries, (a) the inner product scores exhibit minor variations within a narrow range, and then the upsampling kernels for these neighboring nine pixels are highly similar, weakening the discrimination of feature semantics. However, (b) our PCDC-Block generates considerably more discriminative upsampling kernels that are more accurately aligned with the boundary structures and can effectively alleviate the blurring issue.

Remark 3: Compared with the conventional inner product operator in Eq. (3), the proposed PCDC-Block-based similarity calculation has specific merits: 1) With the well-aligned query-key pair containing similar local contents as inputs, such a paired central difference design is inherently well-suited for manifesting the similarity between \bar{q} and \bar{k} , and is proficient in detecting intricate structural details; 2) The incorporation of learnable weights makes the similarity computation more flexible, which is helpful for accurate upsampling. The performance gains brought by these advantages will be validated in Sec. 5.3.2.

4.3 Fine-grained Neighbor Selection

From Sec. 3, for the similarity-based feature upsampling pipeline, the neighborhood selection $\mathcal{N}(i)$ exists in two procedures, *i.e.*, 1) the selection on key feature for query-key similarity calculation and 2) the selection on value feature for the weight-value computation in Eq. (2). For the existing approaches implemented based on Eqs. (2)(3), they select the neighbors $\mathcal{N}(i)$ directly on LR key feature \bar{k} and LR value feature x in a grid-wise manner, respectively. This would possibly result in mosaic artifacts as analyzed in Sec. 3. To address this problem, for our proposed refreshed pipeline mainly implemented based on Eqs. (2) (9) (12),

we develop a simple yet effective fine-grained neighbor selection (FNS) strategy and choose $\mathcal{N}(i)$ on HR key feature (i.e., \mathbf{k} or \mathbf{q}_{GS}) for Eq. (12) and HR value feature (i.e., bilinearly upsampled \mathbf{x}) for Eq. (2), respectively.

To understand our FNS strategy more intuitively, Fig. 7 presents the computation process of similarity score for the query-key pair under a simplified case where the kernel size $K = 1$ and each query pixel would pair with only one neighboring pixel in the key feature. As seen, for the case without FNS, all the four HR query elements in the red dotted box would pair with the same neighboring LR key element to compute the similarity score. However, for our proposed FNS, the neighbor selection is executed on the bilinearly upsampled HR key feature rather than the original LR one. In this manner, the four HR query elements would separately pair with different neighboring HR key elements, as marked by four red dotted boxes. Such a smoother query-key pair selection manner would promote the smoothness of similarity scores for adjacent HR query pixels with different neighbors in the key feature. These advantageous characteristics of FNS can be readily extended to scenarios with larger kernel sizes. Albeit simple, this FNS strategy can be implemented efficiently without introducing any additional computational cost, and can fundamentally eliminate mosaic artifacts, which can be observed by comparing the upsampled features $\tilde{\mathbf{x}}$ in Figs. 2 (a) and (b). Please refer to Fig. 17 for more experimental validation.

In practical implementation, 1) for Eq. (12), the FNS strategy can be seamlessly combined with the PCDC layer by executing PCDC with a dilation rate equal to the up-sampling ratio; 2) To adopt our FNS in Eq. (2), a naive implementation is to bilinearly upsample \mathbf{x} to obtain the HR one. Fortunately, we eliminate this need by technically encapsulating the weight-value computation and the bilinear upsampling within a single CUDA package, which helps avoid explicitly computing the temporary bilinear upsampling results. These careful designs enable the proposed FNS to be easily encapsulated into different backbones.

Remark 4: Overall, for the three key components in Eqs. (2)(3), we systematically reform the similarity-based upsampling methodology. Specifically, we explicitly optimize the query-key alignment for facilitating the computation of s_i , design a flexible similarity function $\text{sim}(\cdot, \cdot)$, and develop a fine-grained neighbor selection strategy for $\mathcal{N}(i)$ as derived in Secs. 4.1, 4.2, and 4.3, respectively. We accordingly construct a refreshed similarity-based feature upsampler, named ReSFU (see Fig. 2 (b)). Notably, the proposed three designs harmoniously form an inseparable whole with each part being indispensable (see Sec. 5.3.2). The specific and meticulous design of each part ultimately enables ReSFU to be applicable to different network structures, which will be validated in the experiments below.

5 EXPERIMENTS

In this section, we comprehensively substantiate the applicability of our proposed ReSFU by conducting extensive experiments on various network structures for the semantic segmentation task. Then, we provide detailed model verification and ablation studies to clearly show the working mechanism of ReSFU and validate the rationality of every

involved component. Finally, in order to better demonstrate the universality of the proposed ReSFU, we extend it to more application scenarios with a variety of datasets, including medical image segmentation, instance segmentation and panoptic segmentation.

5.1 Experimental Setup

Implementation details. For similarity calculation in Eq. (12), the number of output channels L and groups G are 32 and 4, respectively. The projection dimension D is 32 and the kernel size K is 3. For all the involved networks, we modify the default upsampling method (nearest neighbor for FPN neck [60] or bilinear for other networks) by substituting it with alternative upsamplers (replacement details are described in the experimental comparisons below), while keeping other training settings constant for end-to-end training on NVIDIA V100 GPUs. Please refer to the supplementary material for more details.

Comparison methods. Consistent to the latest works [13], [22], we compare the proposed ReSFU with the following feature upsamplers along this research field, including:

- Deconvolution. It can be executed via the function ‘ConvTranspose2d’ in PyTorch with the kernel size and stride number set to the upsampling ratio.
- Pixelshuffle [8]. It consists of a convolution layer for channel expansion and a reshape process for the element reorganization between the channel dimension and the spatial dimension.
- Stack-JBU [22]. It is a parameterized version of joint bilateral upsampler (JBU) [23] adopted in FeatUp [22]. As analyzed in Sec. 2, the entire multi-view framework in FeatUp is orthogonal to our upsampling design. Hence, we only compare with the upsampler module in FeatUp.
- CARAFE [7]. We adopt its default setting with the kernel size as 3.
- IndexNet [19]. Following [13], we select its ‘HIN’ version. Please note that IndexNet was initially conceived for strict encoder-decoder-based backbones.
- FADE [12]. Since its gating version requires that the guidance feature has the same channel size as the encoder feature, we choose its no-gating version.
- SAPA [2]. Following [13], [22], we use its base version for better stability where the kernel size is 5.
- DySample [13]. We select its ‘S+’ version due to its better overall performance on different network structures as presented in [13].

5.2 Semantic Segmentation on Various Architectures

In this section, for the semantic segmentation task, we verify the effectiveness of our proposed ReSFU by conducting comprehensive experiments on various network structures with different types of popular backbones including ResNet [61], Vision Transformer (ViT) [40], Mix Transformer (MiT) [1], and Swin Transformer [62]. For the selection of network structures, we consider not only the hierarchical upsampling manner adopted by the existing baselines, e.g., SegFormer [1], but also the non-hierarchical upsampling

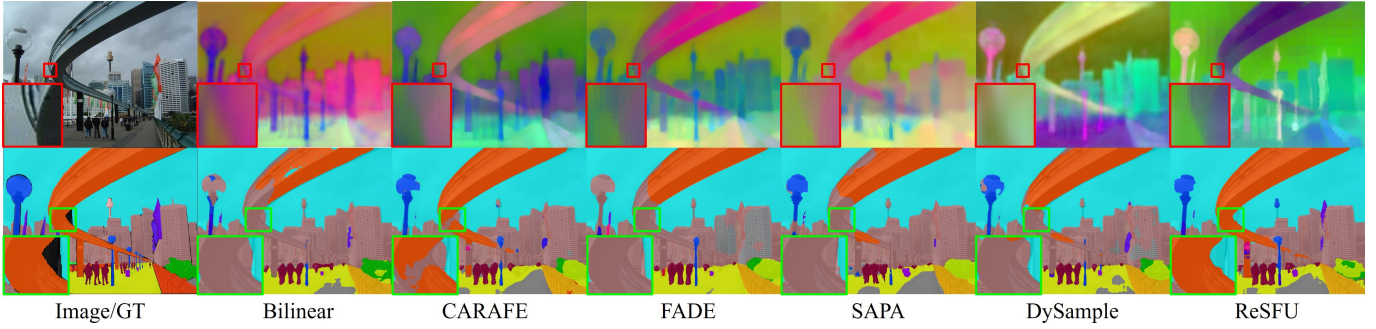


Figure 8: Visual comparison of the $\times 4$ upsampled features \tilde{x} (top) and predicted masks (bottom) on PSPNet-ResNet101.

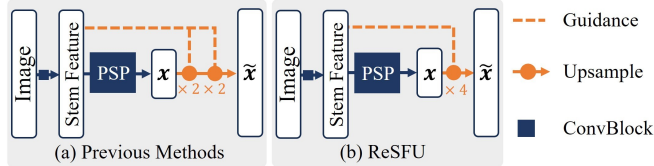


Figure 9: For the CNN-based PSPNet with non-hierarchical upsampling, (a) previous baselines adopt a two-step upsampling by default; (b) Our ReSFU performs a one-step $\times 4$ upsampling. The guidance feature is from the involved stem ConvBlock layer in the ResNet backbone.

Table 1: Evaluation on ADE20K with PSPNet-ResNet50 and PSPNet-ResNet101. The best and second-best results are highlighted in bold and underlined, respectively.

Method	PSPNet-ResNet50				PSPNet-ResNet101			
	mIoU	mAcc	bIoU	Params	mIoU	mAcc	bIoU	Params
Bilinear	41.13	51.41	26.01	46.68M	43.57	54.51	28.28	65.67M
Deconv	39.11	48.79	24.09	50.87M	41.74	51.53	26.65	69.87M
PixelShuffle [8]	38.31	47.78	23.77	50.88M	41.39	50.95	26.64	69.87M
Stack-JBU [22]	41.68	<u>52.69</u>	25.78	46.95M	43.93	54.90	28.34	65.95M
CARAFE [7]	<u>42.06</u>	52.41	26.96	46.86M	<u>44.46</u>	<u>55.47</u>	29.09	65.85M
FADE [12]	41.80	52.07	26.77	46.78M	43.84	53.63	<u>29.36</u>	65.77M
SAPA [2]	41.76	52.32	<u>26.99</u>	46.72M	44.25	55.24	29.18	65.71M
DySample [13]	41.36	51.94	26.10	46.68M	43.99	54.63	28.33	65.67M
ReSFU	42.64	53.26	27.89	46.73M	45.19	56.29	29.87	65.72M

manner, *e.g.*, PSPNet [37] and Segmenter [3], as well as MaskFormer with the FPN head [51], covering most of the existing architecture types involving feature upsampling. Following [2], [13], the semantic segmentation experiments are evaluated using the single-scale testing on the ADE20K dataset [63], which is a widely adopted large-scale scene parsing dataset containing over 20,000 images with pixel-level annotations for 150 object categories. Three typical metrics are used for quantitative evaluation, including mean IoU (mIoU), mean pixel accuracy (mAcc), and boundary IoU (bIoU) [64]. For the bIoU computation, the pixel distance is set to 2% [64]. More experiments on more datasets are provided in the supplementary material.

5.2.1 Evaluation on PSPNet with ResNet Backbone

Upsampling Details. We first select the representative PSPNet [37] with the pioneering CNN-based backbone ResNet [61] for the semantic segmentation task. Fig. 9 presents the replacement manners of different upsampling methods. As seen, for the feature x extracted in the last block, to achieve the $\times 4$ upsampling for the final segmentation output, previous upsamplers adopt two successive $\times 2$ upsampling processes by default. In contrast, our ReSFU

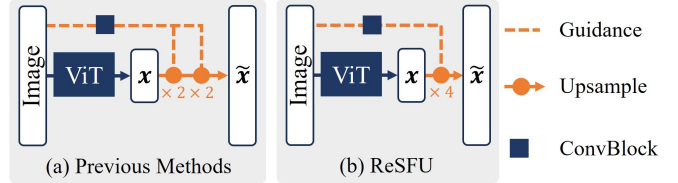


Figure 10: For the Transformer-based Segmenter with non-hierarchical upsampling, (a) previous methods adopt two $\times 2$ upsampling processes; (b) Our ReSFU directly performs a $\times 4$ upsampling. The guidance HR feature is obtained by applying an additional ConvBlock to the input image.

is simply embedded with a direct $\times 4$ upsampling. For guidance-based upsamplers, *e.g.*, FADE, SAPA, and ReSFU, the guidance feature is from the stem convolution block.

Performance Comparison. Table 1 reports the quantitative results on ADE20K with two variants of the ResNet backbone, *i.e.*, ResNet50 and ResNet101. It is clearly observed that with the comparable number of network parameters, our proposed ReSFU consistently outperforms other upsampling approaches in three metrics, *i.e.*, mIoU/mAcc/bIoU (%). Taking PSPNet-ResNet101 as an example, Fig. 8 presents the upsampled features \tilde{x} and the corresponding segmentation results obtained with different upsamplers.² From the feature visualizations, we can find that the object boundary upsampled by our ReSFU is much clearer, thus boosting more accurate segmentation results. In comparison with other approaches with multi-step $\times 2$ upsampling processes, even with a direct one-step high-ratio upsampling, our proposed ReSFU can still obtain superior performance, which facilitates the deployment in practical applications.

5.2.2 Evaluation on Segmenter with ViT Backbone

Upsampling Details. Here we introduce the representative ViT-based network, Segmenter [3] with the FCN-head [4], and present the incorporation manners of different feature upsampling methods as depicted in Fig. 10. Similar to PSPNet, other baselines are inserted in an iterative $\times 2$ upsampling manner while the proposed ReSFU is operated with a direct high-ratio upsampling. To generate the guidance, we apply an extra ConvBlock to the input image in order

²For feature visualization in all the experiments, we follow [22] and adopt principal component analysis [65] to reduce the features to three channels corresponding to the RGB values. Note that since the feature extractors are not frozen and are trained together with different upsamplers, there may be significant variations in color tone across different feature visualizations.

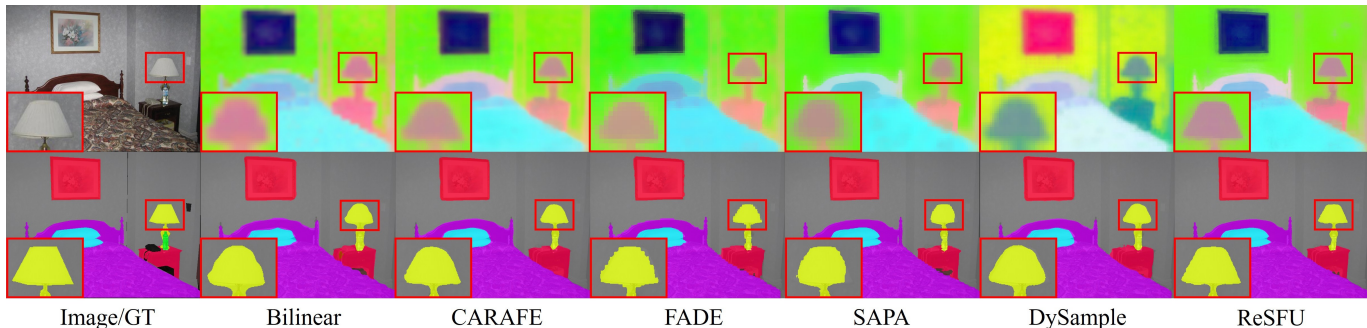


Figure 11: Visual comparison of the $\times 4$ upsampled features \tilde{x} (top) and predicted masks (bottom) with Segmenter-ViT-S.

Table 2: Evaluation on ADE20K with Segmenter-ViT-S and Segmenter-ViT-L. The best and second-best results are highlighted in bold and underlined, respectively.

Method	Segmenter-ViT-S				Segmenter-ViT-L			
	mIoU	mAcc	bloU	Params	mIoU	mAcc	bloU	Params
Bilinear	45.75	56.88	27.82	22.04M	50.96	62.05	33.07	304.17M
Deconv	40.93	51.62	23.77	24.40M	50.01	61.14	31.75	321.67M
PixelShuffle [8]	41.24	52.37	23.87	24.41M	50.50	61.49	31.45	321.69M
Stack-JBU [22]	45.70	56.86	27.84	22.20M	51.03	62.39	32.90	305.96M
CARAFE [7]	<u>46.25</u>	<u>57.63</u>	<u>28.99</u>	22.21M	51.85	62.96	<u>34.49</u>	305.14M
FADE [12]	45.71	56.81	28.72	22.14M	50.07	61.79	33.32	305.08M
SAPA [2]	45.79	57.36	28.97	22.09M	51.20	62.46	33.31	304.99M
DySample [13]	45.78	56.88	28.37	22.09M	<u>52.04</u>	<u>63.27</u>	34.17	305.02M
ReSFU	46.97	57.91	29.96	22.11M	52.56	63.63	35.27	304.98M

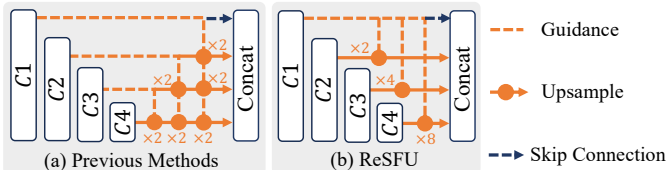


Figure 12: For SegFormer with hierarchical upsampling, (a) previous baselines execute the iterative $\times 2$ upsampling with utilizing C_3 , C_2 , and C_1 as the guidance feature, respectively; (b) Our ReSFU only adopts the guidance C_1 for the direct upsampling with different ratios.

to obtain a shallow HR feature. The ConvBlock consists of “Conv3 \times 3+GroupNorm+ReLU+Conv3 \times 3” layers, with the channel dimension being “3 \rightarrow 64 \rightarrow 32”.

Performance Comparison. For comprehensiveness, we evaluate our ReSFU based on the ViT backbone with different sizes, *e.g.*, ViT-S and ViT-L. As reported in Table 2, the proposed ReSFU evidently surpasses other methods, and achieves the best mIoU/mAcc/bIoU (%) scores under different backbones with the comparable number of parameters. The visual comparison is presented in Fig. 11, clearly showing that our proposed ReSFU achieves better feature upsampling effects with more accurate delineation of object boundaries, *e.g.*, the desk lamp. These findings effectively validate the suitability of our ReSFU in the current popular Transformer-based architectures, demonstrating its strong potential for practical application.

5.2.3 Evaluation on SegFormer with MiT

Upsampling Details. For the semantic segmentation task, SegFormer [1] is another mainstream Transformer-based network structure. Different from Segmenter with a non-hierarchical upsampling architecture, the upsampling process in SegFormer is composed of hierarchical forms among

Table 3: Evaluation on ADE20K with SegFormer-MiT-B1 and SegFormer-MiT-B5. The best and second-best results are highlighted in bold and underlined, respectively.

Method	SegFormer-MiT-B1				SegFormer-MiT-B5			
	mIoU	mAcc	bloU	Params	mIoU	mAcc	bloU	Params
Bilinear	40.97	51.73	24.89	13.72M	49.13	60.69	32.32	82.01M
Deconv	40.73	51.25	23.78	15.29M	49.76	61.39	32.95	83.52M
PixelShuffle [8]	39.69	50.11	23.55	15.30M	50.09	61.69	33.11	83.59M
Stack-JBU [22]	41.71	52.01	25.80	13.95M	49.53	60.72	32.89	82.24M
CARAFE [7]	42.75	53.96	27.09	14.16M	<u>50.45</u>	62.29	33.78	82.45M
IndexNet [19]	41.79	52.40	25.45	26.32M	49.73	61.32	33.21	94.61M
FADE [12]	43.09	<u>53.89</u>	28.33	14.00M	50.43	61.99	34.51	82.29M
SAPA [2]	42.74	53.39	27.61	13.82M	49.61	61.11	34.02	82.11M
DySample [13]	<u>43.48</u>	53.82	27.38	13.72M	50.14	61.51	33.93	82.01M
ReSFU	43.84	54.75	<u>28.06</u>	13.86M	50.89	<u>62.00</u>	<u>34.40</u>	82.15M

different levels of features. As displayed in Fig. 12, the encoder outputs four levels of features, *i.e.*, C_1 , C_2 , C_3 , and C_4 with different resolutions. The LR features C_2 , C_3 , and C_4 require a $\times 2$, $\times 4$, and $\times 8$ upsampling, respectively, to be concatenated with the HR C_1 together for the final segmentation. For the existing upsamplers, they iteratively perform the multi-step $\times 2$ upsampling. For instance, to upsample the LR feature C_4 to the same resolution as C_1 , the guidance-based upsampling methods, *e.g.*, FADE and SAPA, sequentially execute three $\times 2$ upsampling procedures by adopting the adjacent-level features C_3 , C_2 and C_1 as guidance, respectively. However, for our ReSFU, no matter which level the feature is at, only one direct high-ratio upsampling is utilized under the fixed guidance of C_1 , thus halving the total number of upsampling modules.

Performance Comparison. Table 3 lists the quantitative results on two variants of the backbone MiT, *i.e.*, MiT-B1 and MiT-B5, and the proposed ReSFU achieves better overall performance on all these metrics. Fig. 13 illustrates the $\times 8$ upsampled feature \tilde{C}_4 and the segmentation result obtained by different upsamplers. We can observe that for the comparing approaches with three consecutive $\times 2$ upsampling modules, *e.g.*, CARAFE and DySample, the final upsampled features exhibit blurry effects. Nevertheless, even with a simpler $\times 8$ upsampling module, our ReSFU still accomplishes better detail preservation without mosaic artifacts. These favorable effects are mainly attributed to the careful designs of the controllable feature alignment and the fine-grained neighbor selection process, which enables ReSFU to be suitable for this direct high-ratio upsampling scenario. Thus, different from the current guidance-based feature upsampling methods, our ReSFU does not require features of adjacent levels as guidance, which naturally makes it

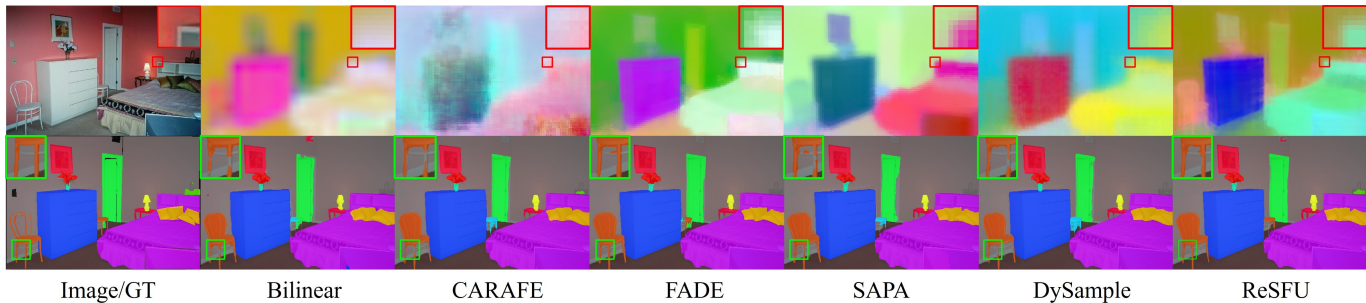


Figure 13: Visual comparison of the $\times 8$ upsampled features \tilde{C}_4 and predicted masks with SegFormer-MiT-B5.

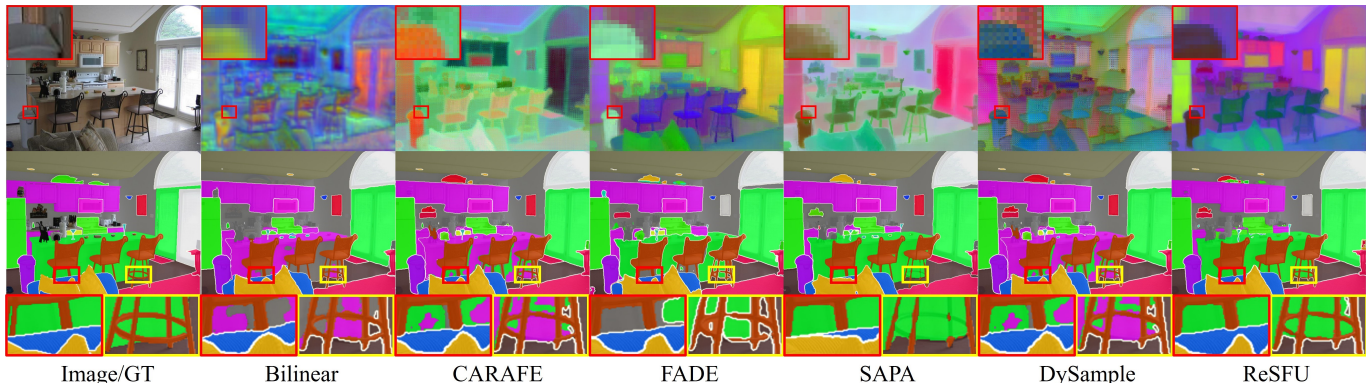


Figure 14: Visual comparison of the upsampled features P_2 in Fig. 15 and predicted masks with MaskFormer-Swin-L.

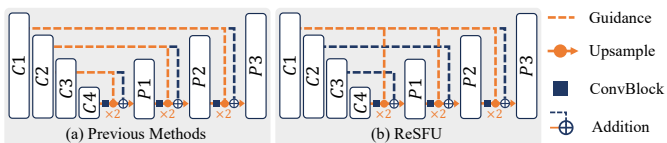


Figure 15: For MaskFormer with the FPN neck, (a) previous methods sequentially take C_3 , C_2 , and C_1 as guidance to execute the $\times 2$ upsampling; (b) Our ReSFU directly utilizes C_1 to guide the upsampling for different levels of features.

possible to be extended to more network architectures not limited to hierarchical upsampling.

5.2.4 Evaluation on MaskFormer with Swin-Transformer

Upsampling Details. MaskFormer [51] is also a cutting-edge Transformer-based network for the segmentation task. It contains a FPN neck-based upsampling module [60], different from that adopted in Segmenter and SegFormer. As presented in Fig. 15, the FPN neck consists of three $\times 2$ upsampling procedures. For the guidance-based comparing methods, they regard the adjacent-level features, *i.e.*, C_3 , C_2 , and C_1 , as the guidance for these three $\times 2$ upsampling modules, respectively. However, for ReSFU, we always utilize the relatively shallower feature C_1 as guidance to introduce more information with details.

Performance Comparison. First, we quantitatively evaluate all the comparing methods based on two versions of Swin Transformer [62] with varying sizes, including Swin-B and Swin-L. As observed from Table 4, ReSFU consistently obtains state-of-the-art outcomes over all metrics. Then based on MaskFormer-Swin-L, we visualize the HR features upon upsampling P_2 . From the upper row in Fig. 14, it is clearly seen that the comparing methods suffer from either blurriness or checkerboard artifacts [66]. In contrast, our

Table 4: Evaluation on ADE20K with MaskFormer-Swin-B and MaskFormer-Swin-L. The best and second-best results are highlighted in bold and underlined, respectively.

Method	MaskFormer-Swin-B				MaskFormer-Swin-L			
	mIoU	mAcc	bIoU	Params	mIoU	mAcc	bIoU	Params
Nearest	52.56	65.76	37.41	101.83M	53.94	66.13	39.02	211.58M
Bilinear	52.99	66.33	37.19	101.83M	53.86	66.21	38.46	211.58M
Stack-JBU [22]	53.53	66.57	37.53	101.91M	54.22	<u>67.26</u>	38.44	211.66M
CARAFE [7]	53.70	66.79	38.31	102.05M	<u>54.48</u>	67.12	39.06	211.80M
FADE [12]	53.69	66.12	<u>38.35</u>	101.97M	54.47	66.59	<u>39.46</u>	211.72M
SAPA [2]	<u>53.87</u>	<u>66.87</u>	37.97	101.88M	54.41	66.40	39.20	211.63M
DySample [13]	53.62	66.77	38.12	101.83M	54.17	67.13	39.22	211.58M
ReSFU	54.66	68.25	38.69	101.97M	55.33	68.64	39.58	211.72M

ReSFU can generate clearer object boundaries and preserve more useful content, which in turn promotes better mask prediction as shown in the lower row.

5.3 Model Analysis

To better understand the working mechanism underlying the proposed ReSFU and validate the rationality of each methodological design, in this section, we conduct a comprehensive model analysis experiment, including model visualization and a series of ablation studies.

5.3.1 Model Visualization

Based on the backbone Segmenter-ViT-S in Fig. 10 (b), we first visualize each component learned by ReSFU.

Visualization of Query-Key Features. Fig. 16 (a) presents each component, including original features y and x , two aligned query-key pairs (q_{GF} and \tilde{k} , q and q_{GS}), and the upsampled feature \tilde{x} . It is clearly observed that the GF-based optimization query q_{GF} semantically resembles \tilde{k} while retaining structural information in q , *e.g.*, the edges of the tower. The smoothed query q_{GS} effectively removes

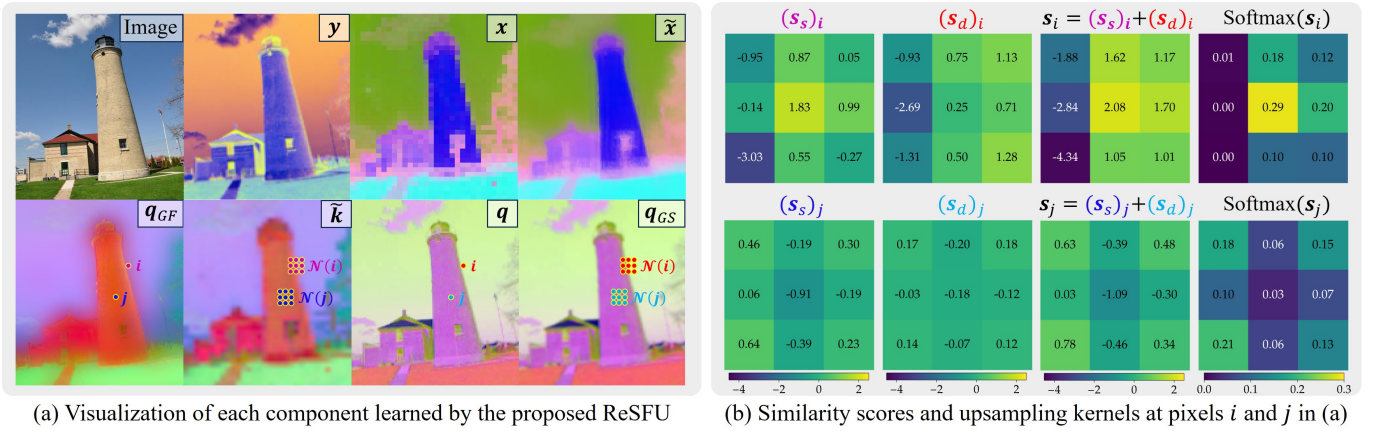


Figure 16: Visualization verification about the working mechanism underlying ReSFU based on Segformer-ViT-S.

Table 5: Ablation study on the query-key feature alignment in Sec. 4.1 with the similarity measurement $\text{sim}(\cdot, \cdot)$ implemented by the PCDC block in Sec. 4.2 and the neighbor selected via the FNS strategy in Sec. 4.3.

Variant	Feature Alignment				Similarity Score s	Segformer-ViT-S				SegFormer-MiT-B1			
	s_s	q_{GF}	s_d	q_{GS}		mIoU	mAcc	bloU	Params	mIoU	mAcc	bloU	Params
(a)	X	X	X	X	Bilinear	45.75	56.88	27.82	22.04M	40.97	51.73	24.89	13.72M
(b)	✓	X	X	X	$s = s_s = \text{sim}(q, \tilde{k})$	46.30	57.45	29.47	22.09M	43.26	54.07	27.76	13.81M
(c)	✓	✓	X	X	$s = s_s = \text{sim}(q_{GF}, \tilde{k})$	46.51	57.89	29.66	22.09M	43.68	54.36	28.13	13.81M
(d)	X	X	✓	X	$s = s_d = \text{sim}(q, q)$	46.21	57.35	29.13	22.07M	42.91	53.60	27.43	13.79M
(e)	X	X	✓	✓	$s = s_d = \text{sim}(q, q_{GS})$	46.48	57.52	29.47	22.07M	43.02	53.83	27.57	13.79M
(f)	✓	✓	✓	✓	$s = (c) s_s + (e) s_d$	46.97	57.91	29.96	22.11M	43.84	54.75	28.06	13.86M

Table 6: Ablation study on similarity measurement $\text{sim}(\cdot, \cdot)$.

Variant	Similarity Measurement $\text{sim}(\cdot, \cdot)$	Segformer-ViT-S				SegFormer-MiT-B1			
		mIoU	mAcc	bloU	Params	mIoU	mAcc	bloU	Params
(a)	Inner Product in Eq. (3)	45.86	56.92	28.14	22.08M	42.35	53.06	26.97	13.77M
(b)	PCDC in Fig. 5 \rightarrow Conv (concat(\tilde{q}, \tilde{k}))	46.59	57.85	29.69	22.12M	42.88	53.52	27.88	13.91M
(c)	PCDC-Block in Fig. 5	46.97	57.91	29.96	22.11M	43.84	54.75	28.06	13.86M

minor noises in the original query q within the semantically consistent regions, such as the lawn. Attributed to such rational alignment in both the detail and semantic spaces, the upsampled HR feature \tilde{x} maintains semantic fidelity to the original LR feature x , while finely preserving distinguishable edges and removing mosaic artifacts. All these visualization results exhibit desirable effects and comply with our design motivations.

Visualization of Upsampling Kernels. Fig. 16 (b) further presents the PCDC-Block-based similarity scores s_s for the pair q_{GF} and \tilde{k} , and s_d for the pair q and q_{GS} , and the upsampling kernels $\text{Softmax}(s)$ at two representative locations, *i.e.*, pixel i near the object boundary and pixel j in the smooth region. Concretely, 1) for pixel i belonging to the class category of ‘sky’, we can observe that $(s_s)_i$ and $(s_d)_i$ effectively collaborate to generate a rational upsampling kernel $\text{Softmax}(s_i)$ that assigns negligible weights to the left region representing the semantics of ‘tower’; 2) For pixel j , $(s_s)_j$ and $(s_d)_j$ are smoother than the scores for pixel i , complying with the smoothness of this region. Besides, we discover that the scores at four corners are slightly higher. This is mainly attributed to the flexible learning capability of PCDC-Block, which has the potential to adaptively detect the smoothness of the location and correspondingly produce

more stable and smoother upsampling results by evenly assigning more weights to the far-away feature elements.

5.3.2 Ablation Study

Based on the non-hierarchical Segformer-ViT-S and the hierarchical SegFormer-MiT-B1, we conduct a series of ablation studies to fully verify the role of each design in ReSFU, including feature alignment in the semantic space and the detail space, paired central difference convolution (PCDC) block for similarity calculation, and fine-grained neighbor selection (FNS) strategy.

Ablation Study on Feature Alignment. Here we execute a fine-grained ablation study on the query-key feature alignment in Sec. 4.1, including s_s in Eq. (7) and s_d in Eq. (8), as well as the designs, *i.e.*, guided filter-based optimized query q_{GF} and Gaussian smoothed detail-space key q_{GS} .

Table 5 reports the quantitative results under different variants, where the variant (f) is exactly our proposed ReSFU. Specifically, compared with the bilinear upsampler (a), the performance gains achieved by variant (b) and variant (d) correspondingly validate that the introduction of the semantic-aware mutual similarity s_s and the detail-aware self-similarity s_d are beneficial for improving the segmentation performance, respectively. From the comparison

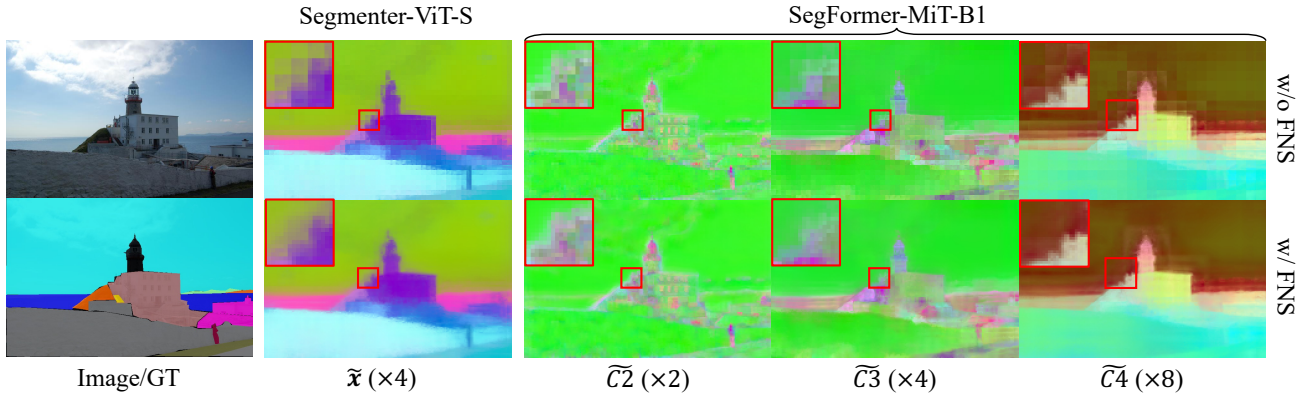


Figure 17: Effect of FNS on upsampled features extracted by Segmenter-ViT-S and SegFormer-MiT-B1.

Table 7: Ablation study on the neighbor selection manner.

Neighbor Selection	Segmenter-ViT-S			SegFormer-MiT-B1		
	mIoU	mAcc	bIoU	mIoU	mAcc	bIoU
w/o FNS	46.80	57.78	29.70	43.12	53.70	27.24
w/ FNS	46.97	57.91	29.96	43.84	54.75	28.06

Table 8: Ablation study about hyperparameters based on Segmenter-ViT-S. ‘†’ denotes the default setting for ReSFU.

Hyperparameter		mIoU	mAcc	bIoU	Params	FLOPs
Kernel Size	† K=3	46.97	57.91	29.96	22.11M	33.88G
	K=5	46.99	57.90	30.39	22.14M	34.49G
	K=7	47.02	58.37	30.41	22.20M	35.39G
Projection Dimension	D=16	46.58	58.09	29.88	22.09M	33.63G
	† D=32	46.97	57.91	29.96	22.11M	33.88G
	D=64	47.00	58.35	30.18	22.14M	34.39G
Group	G=1	47.06	57.97	30.36	22.19M	35.29G
	G=2	47.01	58.05	30.22	22.13M	34.35G
	† G=4	46.97	57.91	29.96	22.11M	33.88G
	G=8	46.71	57.97	29.94	22.09M	33.65G

between (b) and (c), it is easily known that the proposed guided filter-based feature alignment in the semantic space can indeed further boost s_s for more accurate segmentation. By comparing (d) with (e), we can find that the utilization of a smoothed key in the detail space can indeed bring slight performance improvement without any additional cost, which finely complies with the analysis in Sec. 4.1.2.

Ablation Study on Similarity Measurement. To comprehensively validate the effectiveness of our proposed PCDC-Block, we compare three different similarity measurements $\text{sim}(\cdot, \cdot)$, including (a) traditional inner product in Eq. (3); (b) replacing the PCDC layer in Fig. 5 with a vanilla convolution by inputting the concatenation of \bar{q} and \bar{k} ; (c) PCDC-Block in Fig. 5. From the results in Table 6, it is observed that the proposed PCDC-Block has the better capability to capture the relations between query-key pairs for precise similarity calculation and thus promotes the segmentation accuracy. Considering the evident gains over (a), the slight computational cost brought by our method is acceptable. Please refer to supplementary material for visual results.

Ablation Study on Neighbor Selection. Table 7 reports the effect of FNS on the segmentation performance achieved

Table 9: Comparisons on FLOPs and the number of parameters, where FLOPs are tested with images of size 512×512 .

Method	Segmenter-ViT-S		Method	Segmenter-ViT-S	
	FLOPs	Params		FLOPs	Params
Bilinear	32.77G	22.04M	FADE [12]	33.92G	22.14M
Deconv	35.16G	24.40M	SAPA [2]	33.28G	22.09M
PixelShuffle [8]	35.16G	24.41M	DySample [13]	32.90G	22.09M
Stack-JBU [22]	35.32G	22.20M	ReSFU	33.88G	22.11M
CARAFE [7]	32.96G	22.21M	/	/	/

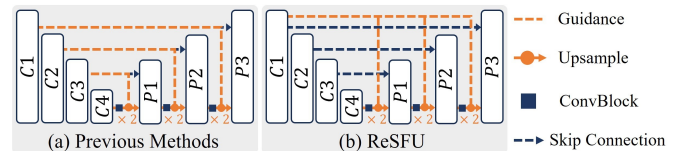


Figure 18: For the U-shape TransUNet, (a) previous methods sequentially use C_3 , C_2 , and C_1 as guidance; (c) ReSFU only uses C_1 as guidance for upsampling at different levels.

by our ReSFU. As seen, without adopting FNS, the model would suffer from a large performance drop, especially for SegFormer with a higher-ratio ($\times 8$) upsampling process as presented in Fig. 12. For better clarity, we provide visual comparisons of upsampled features extracted by these two different network structures. From Fig. 17, we can clearly find that for different levels of features, *i.e.*, x in Segmenter, C_2 , C_3 , and C_4 in SegFormer, their upsampled feature maps without FNS always suffer from severe mosaic effects, especially for larger upsampling ratios. Fortunately, this unfavorable phenomenon can be effectively eliminated by adopting our proposed FNS strategy. It is worth mentioning that as explained in Sec. 4.3, FNS is directly implemented based on bilinearly-upsampled features, and it introduces no extra parameters and computational costs.

Ablation Study on Hyperparameters. Besides, based on Segmenter-ViT-S, we analyze the influence of the key hyperparameters on the segmentation performance, including the kernel size K for neighbor selection, the projection dimension D for generating query-key features, and the number of group G in Eq. (12) for similarity measurement.

The results are reported in Table 8. As observed, a larger kernel size K means that more neighboring pixels would be selected for the more accurate similarity measurement, thereby boosting the performance. However, it would decrease the computation efficiency and incur additional parameters. We select the default kernel size $K = 3$ to balance

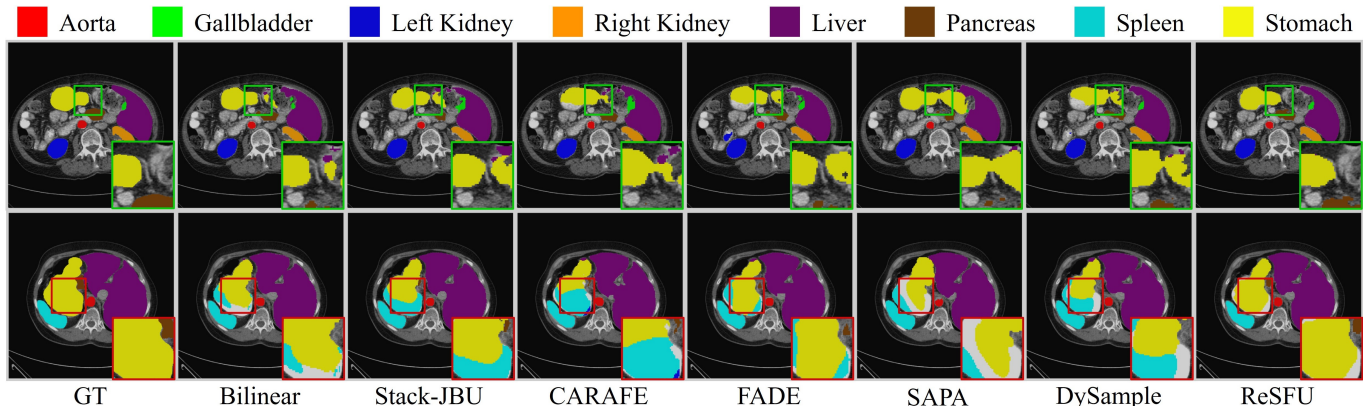


Figure 19: Visual comparison of different feature upsampling methods on the Synapse dataset based on TransUNet.

Table 10: Evaluation on the Synapse dataset annotated with eight abdominal organs based on TransUNet. The best and second-best results are highlighted in bold and underlined, respectively.

Method	Dice (%) (\uparrow)								Average	
	Aorta	Gallbladder	Kidney (L)	Kidney (R)	Liver	Pancreas	Spleen	Stomach	Dice (%) (\uparrow)	HD95 (\downarrow)
Bilinear	87.23	63.13	81.87	77.02	94.08	<u>55.86</u>	<u>85.08</u>	<u>75.62</u>	<u>77.48</u>	31.69
Stack-JBU [22]	87.17	59.13	85.03	78.24	94.20	54.73	83.85	76.36	77.34	30.88
CARAFE [7]	86.34	62.21	83.32	79.31	93.69	52.03	82.06	73.96	76.61	30.89
FADE [12]	86.22	62.56	83.44	77.67	93.41	53.84	83.39	73.65	76.77	30.55
SAPA [2]	84.22	56.91	75.30	71.79	91.41	47.92	81.50	67.25	72.03	35.46
DySample [13]	87.47	61.50	83.00	77.28	94.63	53.63	85.23	74.20	77.12	<u>28.58</u>
ReSFU	86.93	65.30	<u>83.66</u>	<u>78.42</u>	<u>94.61</u>	60.98	84.95	77.31	79.02	25.64

Table 11: Evaluation on the ACDC dataset with TransUNet. The best and second-best results are highlighted in bold and underlined, respectively.

Method	Dice (%) (\uparrow)			Average	
	RV	Myo	LV	Dice (%) (\uparrow)	HD95 (\downarrow)
Bilinear	88.86	<u>84.53</u>	95.73	<u>89.71</u>	2.18
Stack-JBU [22]	88.67	82.83	<u>95.69</u>	89.06	2.09
CARAFE [7]	87.57	83.16	95.38	88.70	2.26
FADE [12]	88.28	84.43	95.96	89.56	2.24
SAPA [2]	87.37	84.01	95.00	88.79	<u>1.90</u>
DySample [13]	<u>88.85</u>	82.96	95.37	89.06	2.75
ReSFU	88.70	85.16	96.26	90.04	1.82

the performance and cost. For the query-key features, we find that a larger D would generate better feature representation, and then benefit the information propagation for the final segmentation. We choose D as 32 by default. The smaller G is, the better it is to capture the relations between query-key pairs, but it brings more computational overhead. In experiments, we set the default group number $G = 4$.

Under the default configurations with $K = 3$, $D = 32$, and $G = 4$, the overhead of our ReSFU is comparable or even lower than other baselines (see Table 9). Taking into account performance, universality, and ease of deployment, our method has a better potential for real applications.

5.4 Application to More Tasks

In this section, we extend ReSFU to more application scenarios including medical image segmentation, instance segmentation, and panoptic segmentation.

5.4.1 Medical Image Segmentation

Upsampling Details. For the medical image segmentation task, we choose the prevalent network, TransUNet [48], with a U-shape architecture different from those presented in Sec. 5.2. As illustrated in Fig. 18, this network contains three $\times 2$ upsampling procedures. For the guidance, other upsamplers sequentially adopt $C3$, $C2$, and $C1$, which is a more suitable setting for them, while our ReSFU only uses the shallow $C1$ for guiding the upsampling at different levels of features.

Performance Comparison. The experiments are executed based on two widely-adopted datasets, *i.e.*, Synapse for multi-organ segmentation,³ and the automated cardiac diagnosis challenge (ACDC).⁴ Specifically, Synapse is annotated with eight abdominal organs, *i.e.*, aorta, gallbladder, spleen, left kidney, right kidney, liver, pancreas, spleen, and stomach. Following [48], we employ 18 computed tomography (CT) scans with 2,212 axial slices for training and 12 CT scans for validation. For ACDC, the involved magnetic resonance imaging (MRI) scans are annotated with left ventricle (LV), right ventricle (RV), and myocardium (MYO). Consistent to [48], we utilize 70 scans with 1,930 axial slices for training and 40 scans for validation. Quantitative evaluation is conducted based on the two typical metrics, including Dice (the higher the better) and the 95-th percentile of the Hausdorff Distance (HD95, the lower the better).

From the results reported in Table 10 for Synapse and Table 11 for ACDC, we can easily conclude that most of the comparing baselines are inferior to the default bilinear upsampler. However, our proposed ReSFU consistently

³<https://www.synapse.org/#Synapse:syn3193805/wiki/217789>

⁴<https://www.creatis.insa-lyon.fr/Challenge/acdc/>

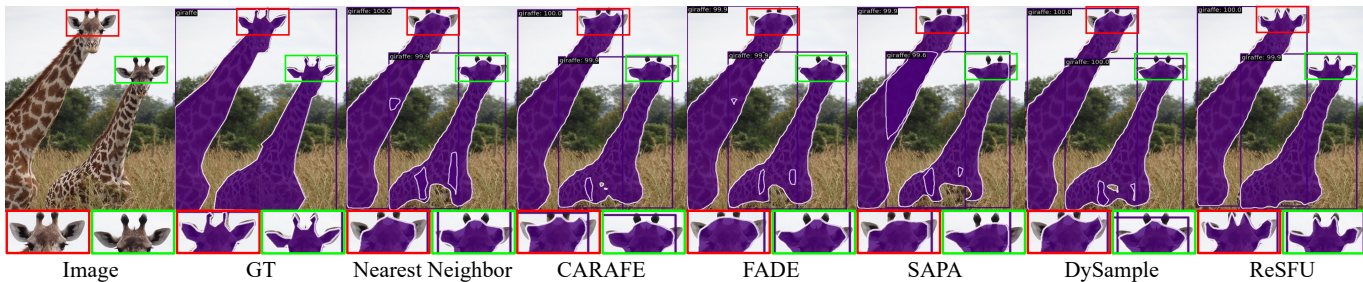


Figure 20: Visualization results of different upsampling methods based on Mask R-CNN for instance segmentation.

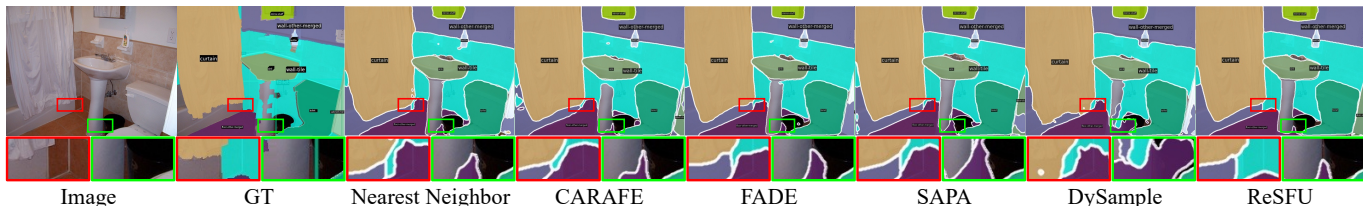


Figure 21: Visualization results of different upsampling methods based on Panoptic FPN for panoptic segmentation.

Table 12: Performance evaluation on two additional segmentation tasks, including instance segmentation and panoptic segmentation. The best and second-best results are highlighted in bold and underlined, respectively.

Method	Instance Segmentation						Panoptic Segmentation				
	AP	AP ₅₀	AP ₇₅	AP _S	AP _M	AP _L	PQ	PQ th	PQ st	SQ	RQ
Nearest	34.7	55.8	37.2	16.1	37.3	50.8	40.2	47.8	28.9	77.8	49.3
Bilinear	34.4	55.4	36.7	15.6	36.9	51.2	40.1	47.5	28.9	77.8	49.1
Deconv	34.5	55.5	36.8	16.4	37.0	49.5	39.6	47.0	28.4	77.1	48.5
PixelShuffle [8]	34.8	56.0	37.3	16.3	37.5	50.4	40.0	47.4	28.8	77.1	49.1
CARAFE [7]	35.4	56.7	37.6	<u>16.9</u>	<u>38.1</u>	51.3	40.8	47.7	30.4	78.2	50.0
IndexNet [19]	34.7	55.9	37.1	16.0	37.0	51.1	40.2	47.6	28.9	77.1	49.3
FADE [12]	35.1	56.7	37.2	16.7	37.5	51.4	40.9	48.0	30.3	78.1	50.1
SAPA [2]	35.1	56.5	37.4	16.7	37.6	50.6	40.6	47.7	29.8	78.0	49.6
DySample [13]	<u>35.5</u>	<u>56.8</u>	<u>37.8</u>	17.0	37.9	<u>51.9</u>	<u>41.1</u>	<u>48.1</u>	<u>30.5</u>	<u>78.2</u>	<u>50.2</u>
ReSFU	36.1	57.4	38.4	16.8	38.8	52.5	41.5	48.4	31.1	78.4	50.7

achieves competitive segmentation performance on different organs, and then obtains the best average accuracy with higher Dice scores and lower HD scores. In Fig. 19, we present the segmentation results on two cases randomly selected from Synapse. As seen, our proposed ReSFU shows the remarkable ability to capture object boundaries with higher segmentation accuracy. These results further demonstrate the satisfactory application potential of ReSFU.

5.4.2 Instance Segmentation and Panoptic Segmentation

Here we further verify the universality of our proposed ReSFU through two other segmentation tasks, including instance segmentation and panoptic segmentation.

Specifically, for instance segmentation, we employ the classic Mask R-CNN [42] with ResNet50 as the backbone and replace the upsampling stages in FPN with ReSFU, as shown in Fig. 15 (b). All the results are quantitatively evaluated based on metrics of the average precision (AP) series, including mask AP, AP₅₀, AP₇₅, AP_S, AP_M, and AP_L. For panoptic segmentation, following [13], we choose Panoptic FPN [6] with ResNet50 as the backbone and adjust the three upsamplers in FPN, as presented in Fig. 15 (b). We report panoptic quality (PQ), PQ on things (PQth), PQ

on stuff (PQst), segmentation quality (SQ), and recognition quality (RQ) [6]. The MS COCO dataset [67] is used for training and evaluating the two tasks.

Table 12 reports the quantitative results on the two additional segmentation tasks. As seen, our proposed ReSFU performs more competitively over almost all the evaluation metrics, showing favorable universality. Fig. 20 and Fig. 21 provide the visual results achieved by different upsampling methods for instance segmentation and panoptic segmentation, respectively. It is easily observed that the proposed ReSFU attains better segmentation results with more details and more consistent semantics, such as the horns and ears of the giraffes in Fig. 20, and the floor in Fig. 21.

5.5 More Discussions on Direct/Iterative Upsampling

As explained previously, other comparing upsamplers are inserted in an iterative $\times 2$ upsampling manner by default, while our proposed ReSFU is always simply executed in a direct upsampling process without iterative guidance features. Here we provide more discussions to further evaluate different methods under different upsampling manners.

Taking PSPNet as an example, for the comparing methods, *e.g.*, CARAFE, FADE, SAPA, DySample, and ReSFU,

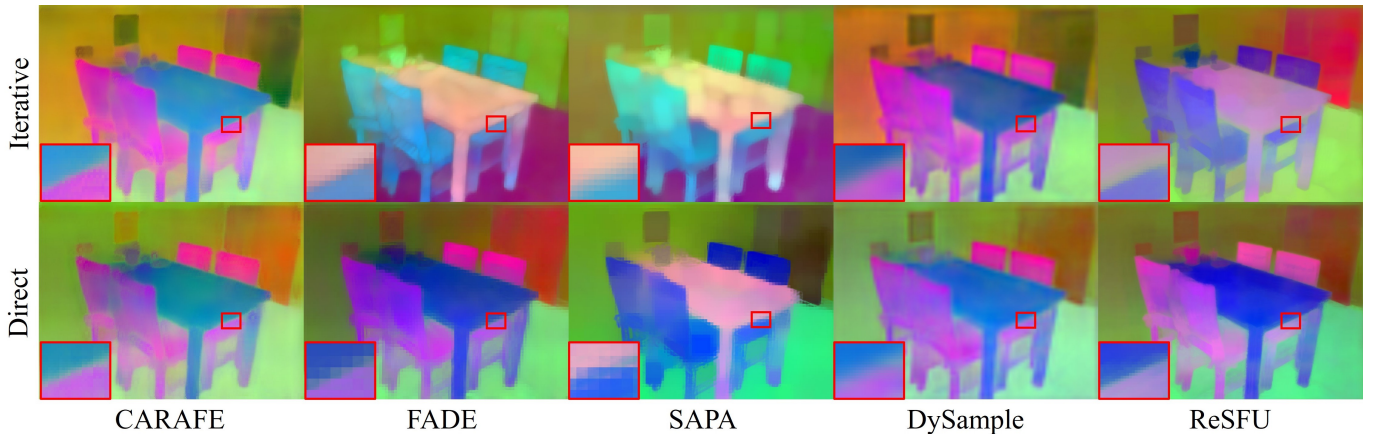


Figure 22: Visual comparison of upsampled features \tilde{x} obtained in an iterative upsampling (Fig. 9 (a)) and a direct $\times 4$ upsampling manners (Fig. 9 (b)) based on PSPNet-ResNet101.

we visually compare their upsampled features \tilde{x} obtained in the iterative $\times 2$ upsampling manner (Fig. 9 (a)) and the direct $\times 4$ upsampling manner (Fig. 9 (b)). As displayed in Fig. 22, with the high-ratio direct upsampling, CARAFE, FADE, SAPA, and DySample generate varying degrees of artifacts with more mosaics or blurrier boundaries compared with the iterative upsampling manner. Therefore, in all the experimental comparisons, we follow the default settings in the existing upsamplers and employ them in an iterative manner for better performance. Besides, we also observe that the proposed ReSFU achieves better visual effects with richer semantics and clearer boundaries under both upsampling manners. Therefore, for ease of deployment, we select the direct high-ratio upsampling manner as the default setting for ReSFU in experiments, which can eliminate the requirement of iterative guidance features.

6 CONCLUSION AND FUTURE WORK

In this paper, for the fundamental upsampling design included in almost all current network architectures, we carefully reformulated the current similarity-based feature upsampling framework and thoroughly analyzed the limitations in methodological designs together with experimental visualizations. For each component involved in this pipeline, we meticulously proposed specific optimization designs and correspondingly constructed a refreshed similarity-based feature upsampling framework, called ReSFU. Through comprehensive model verification and ablation studies, we fully validated the role of each component and clearly shown the working mechanism underlying our proposed ReSFU. Based on different types of network architectures, extensive experiments substantiated the superiority of our proposed ReSFU beyond the existing baselines and demonstrated that our ReSFU can be adapted not only to different upsampling structures with flexible guidance manners but also to different applications, including medical image segmentation, instance segmentation, and panoptic segmentation.

Thanks to the favorable generality of our proposed ReSFU, apart from segmentation tasks, there is great potential to extend it to more applications, such as, the pan-sharpening task [68] or the multispectral and hyperspectral image fusion task [69] with the available HR input images

as guidance. However, for the applications without HR reference images, *e.g.*, image super-resolution [70] and image generation [71], these guidance-based feature upsampling methods, *e.g.*, FADE, SAPA, and our ReSFU, are difficult to apply. This is beyond our focus in this paper and deserves further investigation in our future work.

REFERENCES

- [1] E. Xie, W. Wang, Z. Yu, A. Anandkumar, J. M. Alvarez, and P. Luo, "SegFormer: Simple and efficient design for semantic segmentation with Transformers," in *Advances in Neural Information Processing Systems*, vol. 34, 2021, pp. 12 077–12 090.
- [2] H. Lu, W. Liu, Z. Ye, H. Fu, Y. Liu, and Z. Cao, "SAPA: Similarity-aware point affiliation for feature upsampling," in *Advances in Neural Information Processing Systems*, vol. 35, 2022, pp. 20 889–20 901.
- [3] R. Strudel, R. Garcia, I. Laptev, and C. Schmid, "Segmenter: Transformer for semantic segmentation," in *Proceedings of the IEEE/CVF International Conference on Computer Vision*, 2021, pp. 7262–7272.
- [4] J. Long, E. Shelhamer, and T. Darrell, "Fully convolutional networks for semantic segmentation," in *Proceedings of the IEEE/CVF Conference on Computer Vision and Pattern Recognition*, 2015, pp. 3431–3440.
- [5] A. M. Hafiz and G. M. Bhat, "A survey on instance segmentation: state of the art," *International Journal of Multimedia Information Retrieval*, vol. 9, no. 3, pp. 171–189, 2020.
- [6] A. Kirillov, K. He, R. Girshick, C. Rother, and P. Dollár, "Panoptic segmentation," in *Proceedings of the IEEE/CVF Conference on Computer Vision and Pattern Recognition*, 2019, pp. 9404–9413.
- [7] J. Wang, K. Chen, R. Xu, Z. Liu, C. C. Loy, and D. Lin, "CARAFE: Content-aware reassembly of features," in *Proceedings of the IEEE/CVF International Conference on Computer Vision*, 2019, pp. 3007–3016.
- [8] W. Shi, J. Caballero, F. Huszár, J. Totz, A. P. Aitken, R. Bishop, D. Rueckert, and Z. Wang, "Real-time single image and video super-resolution using an efficient sub-pixel convolutional neural network," in *Proceedings of the IEEE/CVF Conference on Computer Vision and Pattern Recognition*, 2016, pp. 1874–1883.
- [9] H. Gao, H. Yuan, Z. Wang, and S. Ji, "Pixel transposed convolutional networks," *IEEE Transactions on Pattern Analysis and Machine Intelligence*, vol. 42, no. 5, pp. 1218–1227, 2019.
- [10] Z. Wojna, V. Ferrari, S. Guadarrama, N. Silberman, L.-C. Chen, A. Fathi, and J. Uijlings, "The devil is in the decoder: Classification, regression and GANs," *International Journal of Computer Vision*, vol. 127, pp. 1694–1706, 2019.
- [11] Z. Tian, T. He, C. Shen, and Y. Yan, "Decoders matter for semantic segmentation: Data-dependent decoding enables flexible feature aggregation," in *Proceedings of the IEEE/CVF Conference on Computer Vision and Pattern Recognition*, 2019, pp. 3126–3135.
- [12] H. Lu, W. Liu, H. Fu, and Z. Cao, "FADE: Fusing the assets of decoder and encoder for task-agnostic upsampling," in *Proceedings of the European Conference on Computer Vision*. Springer, 2022, pp. 231–247.

- [13] W. Liu, H. Lu, H. Fu, and Z. Cao, "Learning to upsample by learning to sample," in *Proceedings of the IEEE/CVF International Conference on Computer Vision*, 2023, pp. 6027–6037.
- [14] K. He, J. Sun, and X. Tang, "Guided image filtering," *IEEE Transactions on Pattern Analysis and Machine Intelligence*, vol. 35, no. 6, pp. 1397–1409, 2012.
- [15] H. Noh, S. Hong, and B. Han, "Learning deconvolution network for semantic segmentation," in *Proceedings of the IEEE/CVF International Conference on Computer Vision*, 2015, pp. 1520–1528.
- [16] J. Wang, K. Chen, R. Xu, Z. Liu, C. C. Loy, and D. Lin, "CARAFE++: Unified content-aware reassembly of features," *IEEE Transactions on Pattern Analysis and Machine Intelligence*, vol. 44, no. 9, pp. 4674–4687, 2021.
- [17] V. Badrinarayanan, A. Kendall, and R. Cipolla, "SegNet: A deep convolutional encoder-decoder architecture for image segmentation," *IEEE Transactions on Pattern Analysis and Machine Intelligence*, vol. 39, no. 12, pp. 2481–2495, 2017.
- [18] D. Mazzini, "Guided upsampling network for real-time semantic segmentation," in *Proceedings of the British Machine Vision Conference*, vol. 117, 2018, pp. 1–12.
- [19] H. Lu, Y. Dai, C. Shen, and S. Xu, "Indices matter: Learning to index for deep image matting," in *Proceedings of the IEEE/CVF International Conference on Computer Vision*, 2019, pp. 3266–3275.
- [20] Y. Dai, H. Lu, and C. Shen, "Learning affinity-aware upsampling for deep image matting," in *Proceedings of the IEEE/CVF Conference on Computer Vision and Pattern Recognition*, 2021, pp. 6841–6850.
- [21] W. Liu, H. Lu, Y. Liu, and Z. Cao, "On point affiliation in feature upsampling," *arXiv preprint arXiv:2307.08198*, 2023.
- [22] S. Fu, M. Hamilton, L. E. Brandt, A. Feldmann, Z. Zhang, and W. T. Freeman, "FeatUp: A model-agnostic framework for features at any resolution," in *International Conference on Learning Representations*, 2024.
- [23] J. Kopf, M. F. Cohen, D. Lischinski, and M. Uyttendaele, "Joint bilateral upsampling," *ACM Transactions on Graphics*, vol. 26, no. 3, pp. 96–100, 2007.
- [24] Z. Su, M. Pietikäinen, and L. Liu, "From local binary patterns to pixel difference networks for efficient visual representation learning," in *Scandinavian Conference on Image Analysis*. Springer, 2023, pp. 138–155.
- [25] T. Ojala, M. Pietikäinen, and D. Harwood, "A comparative study of texture measures with classification based on featured distributions," *Pattern Recognition*, vol. 29, no. 1, pp. 51–59, 1996.
- [26] F. Juefei-Xu, V. Naresh Boddeti, and M. Savvides, "Local binary convolutional neural networks," in *Proceedings of the IEEE/CVF Conference on Computer Vision and Pattern Recognition*, 2017, pp. 19–28.
- [27] X. Zhang, L. Liu, Y. Xie, J. Chen, L. Wu, and M. Pietikainen, "Rotation invariant local binary convolution neural networks," in *Proceedings of the IEEE/CVF International Conference on Computer Vision Workshops*, 2017, pp. 1210–1219.
- [28] Z. Yu, C. Zhao, Z. Wang, Y. Qin, Z. Su, X. Li, F. Zhou, and G. Zhao, "Searching central difference convolutional networks for face anti-spoofing," in *Proceedings of the IEEE/CVF Conference on Computer Vision and Pattern Recognition*, 2020, pp. 5295–5305.
- [29] Z. Yu, J. Wan, Y. Qin, X. Li, S. Z. Li, and G. Zhao, "NAS-FAS: Static-dynamic central difference network search for face anti-spoofing," *IEEE Transactions on Pattern Analysis and Machine Intelligence*, vol. 43, no. 9, pp. 3005–3023, 2020.
- [30] Z. Yu, Y. Qin, H. Zhao, X. Li, and G. Zhao, "Dual-cross central difference network for face anti-spoofing," in *Proceedings of the 30th International Joint Conference on Artificial Intelligence*, 2021, pp. 1281–1287.
- [31] Z. Yu, B. Zhou, J. Wan, P. Wang, H. Chen, X. Liu, S. Z. Li, and G. Zhao, "Searching multi-rate and multi-modal temporal enhanced networks for gesture recognition," *IEEE Transactions on Image Processing*, vol. 30, pp. 5626–5640, 2021.
- [32] Z. Su, W. Liu, Z. Yu, D. Hu, Q. Liao, Q. Tian, M. Pietikäinen, and L. Liu, "Pixel difference networks for efficient edge detection," in *Proceedings of the IEEE/CVF International Conference on Computer Vision*, 2021, pp. 5117–5127.
- [33] Z. Su, J. Zhang, L. Wang, H. Zhang, Z. Liu, M. Pietikäinen, and L. Liu, "Lightweight pixel difference networks for efficient visual representation learning," *IEEE Transactions on Pattern Analysis and Machine Intelligence*, vol. 45, no. 12, pp. 14956–14974, 2023.
- [34] H. Tan, S. Wu, and J. Pi, "Semantic diffusion network for semantic segmentation," in *Advances in Neural Information Processing Systems*, vol. 35, 2022, pp. 8702–8716.
- [35] O. Ronneberger, P. Fischer, and T. Brox, "U-Net: Convolutional networks for biomedical image segmentation," in *Proceedings of the International Conference on Medical Image Computing and Computer Assisted Intervention*. Springer, 2015, pp. 234–241.
- [36] Ç. Kaymak and A. Uçar, "A brief survey and an application of semantic image segmentation for autonomous driving," *Handbook of Deep Learning Applications*, pp. 161–200, 2019.
- [37] H. Zhao, J. Shi, X. Qi, X. Wang, and J. Jia, "Pyramid scene parsing network," in *Proceedings of the IEEE/CVF Conference on Computer Vision and Pattern Recognition*, 2017, pp. 2881–2890.
- [38] L.-C. Chen, Y. Zhu, G. Papandreou, F. Schroff, and H. Adam, "Encoder-decoder with atrous separable convolution for semantic image segmentation," in *Proceedings of the European Conference on Computer Vision*, 2018, pp. 801–818.
- [39] A. Vaswani, N. Shazeer, N. Parmar, J. Uszkoreit, L. Jones, A. N. Gomez, Ł. Kaiser, and I. Polosukhin, "Attention is all you need," *Advances in Neural Information Processing Systems*, vol. 30, pp. 5998–6008, 2017.
- [40] A. Dosovitskiy, L. Beyer, A. Kolesnikov, D. Weissenborn, X. Zhai, T. Unterthiner, M. Dehghani, M. Minderer, G. Heigold, S. Gelly, J. Uszkoreit, and N. Houlsby, "An image is worth 16x16 words: Transformers for image recognition at scale," in *International Conference on Learning Representations*, 2021.
- [41] M.-H. Guo, C.-Z. Lu, Q. Hou, Z. Liu, M.-M. Cheng, and S.-M. Hu, "SegNeXt: Rethinking convolutional attention design for semantic segmentation," in *Advances in Neural Information Processing Systems*, vol. 35, 2022, pp. 1140–1156.
- [42] K. He, G. Gkioxari, P. Dollár, and R. Girshick, "Mask R-CNN," in *Proceedings of the IEEE/CVF International Conference on Computer Vision*, 2017, pp. 2961–2969.
- [43] Z. Cai and N. Vasconcelos, "Cascade R-CNN: High quality object detection and instance segmentation," *IEEE Transactions on Pattern Analysis and Machine Intelligence*, vol. 43, no. 5, pp. 1483–1498, 2019.
- [44] Z. Huang, L. Huang, Y. Gong, C. Huang, and X. Wang, "Mask scoring R-CNN," in *IEEE Conference on Computer Vision and Pattern Recognition*, 2019.
- [45] Z. Tian, C. Shen, X. Wang, and H. Chen, "BoxInst: High-performance instance segmentation with box annotations," in *Proceedings of the IEEE/CVF Conference on Computer Vision and Pattern Recognition*, 2021, pp. 5443–5452.
- [46] Y. Xiong, R. Liao, H. Zhao, R. Hu, M. Bai, E. Yumer, and R. Urtasun, "Upsnet: A unified panoptic segmentation network," in *Proceedings of the IEEE/CVF conference on computer vision and pattern recognition*, 2019, pp. 8818–8826.
- [47] R. Mohan and A. Valada, "EfficientPS: Efficient panoptic segmentation," *International Journal of Computer Vision*, vol. 129, no. 5, pp. 1551–1579, 2021.
- [48] J. Chen, Y. Lu, Q. Yu, X. Luo, E. Adeli, Y. Wang, L. Lu, A. L. Yuille, and Y. Zhou, "TransUNet: Transformers make strong encoders for medical image segmentation," *arXiv preprint arXiv:2102.04306*, 2021.
- [49] H. Cao, Y. Wang, J. Chen, D. Jiang, X. Zhang, Q. Tian, and M. Wang, "Swin-Unet: Unet-like pure Transformer for medical image segmentation," in *European Conference on Computer Vision*. Springer, 2022, pp. 205–218.
- [50] X. Yan, H. Tang, S. Sun, H. Ma, D. Kong, and X. Xie, "After-UNet: Axial fusion Transformer UNet for medical image segmentation," in *Proceedings of the IEEE/CVF winter conference on applications of computer vision*, 2022, pp. 3971–3981.
- [51] B. Cheng, A. Schwing, and A. Kirillov, "Per-pixel classification is not all you need for semantic segmentation," *Advances in Neural Information Processing Systems*, vol. 34, pp. 17864–17875, 2021.
- [52] B. Cheng, I. Misra, A. G. Schwing, A. Kirillov, and R. Girdhar, "Masked-attention mask Transformer for universal image segmentation," in *Proceedings of the IEEE/CVF Conference on Computer Vision and Pattern Recognition*, 2022, pp. 1290–1299.
- [53] J. Jain, J. Li, M. T. Chiu, A. Hassani, N. Orlov, and H. Shi, "OneFormer: One Transformer to rule universal image segmentation," in *Proceedings of the IEEE/CVF Conference on Computer Vision and Pattern Recognition*, 2023, pp. 2989–2998.
- [54] M. D. Zeiler and R. Fergus, "Visualizing and understanding convolutional networks," in *Proceedings of the European Conference on Computer Vision*. Springer, 2014, pp. 818–833.
- [55] K. He and J. Sun, "Fast guided filter," *arXiv preprint arXiv:1505.00996*, 2015.
- [56] N. R. Draper and H. Smith, *Applied Regression Analysis*. John Wiley & Sons, 1998, vol. 326.

- [57] Q. Xu, W. Zhao, G. Lin, and C. Long, "Self-calibrated cross attention network for few-shot segmentation," in *Proceedings of the IEEE/CVF International Conference on Computer Vision*, 2023, pp. 655–665.
- [58] G. Petschnigg, R. Szeliski, M. Agrawala, M. Cohen, H. Hoppe, and K. Toyama, "Digital photography with flash and no-flash image pairs," *ACM Transactions on Graphics*, vol. 23, no. 3, pp. 664–672, 2004.
- [59] A. Paszke, S. Gross, S. Chintala, G. Chanan, E. Yang, Z. DeVito, Z. Lin, A. Desmaison, L. Antiga, and A. Lerer, "Automatic differentiation in PyTorch," in *NIPS 2017 Workshop on Autodiff*, 2017.
- [60] T.-Y. Lin, P. Dollár, R. Girshick, K. He, B. Hariharan, and S. Belongie, "Feature pyramid networks for object detection," in *Proceedings of the IEEE/CVF Conference on Computer Vision and Pattern Recognition*, 2017, pp. 2117–2125.
- [61] K. He, X. Zhang, S. Ren, and J. Sun, "Deep residual learning for image recognition," in *Proceedings of the IEEE/CVF Conference on Computer Vision and Pattern Recognition*, 2016, pp. 770–778.
- [62] Z. Liu, Y. Lin, Y. Cao, H. Hu, Y. Wei, Z. Zhang, S. Lin, and B. Guo, "Swin Transformer: Hierarchical vision transformer using shifted windows," in *Proceedings of the IEEE/CVF International Conference on Computer Vision*, 2021, pp. 10 012–10 022.
- [63] B. Zhou, H. Zhao, X. Puig, S. Fidler, A. Barriuso, and A. Torralba, "Scene parsing through ADE20k dataset," in *Proceedings of the IEEE/CVF Conference on Computer Vision and Pattern Recognition*, 2017, pp. 633–641.
- [64] B. Cheng, R. Girshick, P. Dollár, A. C. Berg, and A. Kirillov, "Boundary IoU: Improving object-centric image segmentation evaluation," in *Proceedings of the IEEE/CVF Conference on Computer Vision and Pattern Recognition*, 2021, pp. 15 334–15 342.
- [65] H. Abdi and L. J. Williams, "Principal component analysis," *Wiley Interdisciplinary Reviews: Computational Statistics*, vol. 2, no. 4, pp. 433–459, 2010.
- [66] Y. Sugawara, S. Shiota, and H. Kiya, "Checkerboard artifacts free convolutional neural networks," *APSIPA Transactions on Signal and Information Processing*, vol. 8, p. e9, 2019.
- [67] T.-Y. Lin, M. Maire, S. Belongie, J. Hays, P. Perona, D. Ramanan, P. Dollár, and C. L. Zitnick, "Microsoft COCO: Common objects in context," in *Proceedings of the European Conference on Computer Vision*. Springer, 2014, pp. 740–755.
- [68] L. Loncan, L. B. De Almeida, J. M. Bioucas-Dias, X. Briottet, J. Chanussot, N. Dobigeon, S. Fabre, W. Liao, G. A. Licciardi, M. Simoes *et al.*, "Hyperspectral pansharpening: A review," *IEEE Geoscience and Remote Sensing Magazine*, vol. 3, no. 3, pp. 27–46, 2015.
- [69] Q. Xie, M. Zhou, Q. Zhao, Z. Xu, and D. Meng, "MHF-Net: An interpretable deep network for multispectral and hyperspectral image fusion," *IEEE Transactions on Pattern Analysis and Machine Intelligence*, vol. 44, no. 3, pp. 1457–1473, 2020.
- [70] Z. Wang, J. Chen, and S. C. Hoi, "Deep learning for image super-resolution: A survey," *IEEE Transactions on Pattern Analysis and Machine Intelligence*, vol. 43, no. 10, pp. 3365–3387, 2020.
- [71] R. Rombach, A. Blattmann, D. Lorenz, P. Esser, and B. Ommer, "High-resolution image synthesis with latent diffusion models," in *Proceedings of the IEEE/CVF Conference on Computer Vision and Pattern Recognition*, 2022, pp. 10 684–10 695.